Chapter 10

Effects of the stratosphere on the troposphere

Lead Authors: Mark P. Baldwin & Nathan P. Gillett

Co-Authors: Piers M. Forster
Edwin P. Gerber
Michaela I. Hegglin
Alexey Yu. Karpechko
Junsu Kim
Paul J. Kushner
Olaf H. Morgenstern
Thomas Reichler
Seok-Woo Son
Kleareti Tourpali

10.1 Introduction

While the focus of this report is on an evaluation of the stratospheric climate and composition of the CCMVal models, public attention is invariably focused more closely on tropospheric climate and climate change. This chapter therefore investigates how the stratospheric variability and changes simulated by the CCMVal models influence tropospheric climate. The simulation of stratosphere-troposphere coupling by the CCMVal models is validated by comparison with observations, and compared with that of the CMIP3 models, whose simulations of future climate formed the basis of the climate projections of the Intergovernmental Panel on Climate Change (IPCC) (Meehl *et al*., 2007b).

As well as reviewing the influences of past and future stratospheric changes on the troposphere in the CCMVal simulations in this chapter, we also review diagnostic studies of dynamical, radiative and chemical processes coupling the stratosphere and troposphere in an attempt to shed light on these issues.

Increasing observational evidence (*e.g*., Kodera *et al*., 1990) suggests stratospheric processes play an important role in tropospheric climate variability across a wide range of time scales. For example:

- On intraseasonal time scales, observations show that

large amplitude anomalies in the strength of the Northern Hemisphere wintertime stratospheric polar vortex frequently precede long-lived (up to ~two months) changes to the tropospheric circulation (Baldwin and Dunkerton 1999, 2001; Polvani and Waugh, 2004). These changes modulate not only average weather, but also the likelihood of extreme events on time scales longer than the limit of deterministic weather prediction (Thompson *et al*., 2002).

• On interannual time scales, the stratospheric QBO has been found to exhibit a signature in surface climate (Coughlin and Tung, 2001; Thompson *et al*., 2002). A stratospheric role has also been suggested in modulating the tropospheric response to solar forcing (*e.g*., Rind *et al*., 2008) and El Niño/Southern Oscillation (ENSO) variations (Ineson and Scaife, 2009).

• On time scales of several years, volcanic eruptions that inject sulphate aerosols into the stratosphere also noticeably influence tropospheric climate both radiatively and dynamically (Robock and Mao, 1992; Graf *et al*., 1994; Kodera and Yamazaki, 1994; Stenchikov *et al*., 1998; 2004; Hamilton, 2007).

• On decadal time scales, Antarctic ozone depletion appears to have had a demonstrable impact not only on stratospheric temperatures and circulation, but on surface climate as well (Thompson and Solomon, 2002; Gillett and Thompson, 2003; Keeley *et al*., 2007).

To first order, the coupling between the stratosphere and troposphere is mediated by wave dynamics. Planetary-scale Rossby waves, gravity waves, and equatorial Kelvin and mixed Rossby-gravity waves typically originate in the troposphere, propagate upward into the stratosphere, and then dissipate causing variability of the stratospheric flow. The conventional view up to the late 1990s was that the resulting interactions are principally one way, *i.e*., that tropospheric waves influence the stratospheric circulation, but that stratospheric circulation anomalies do not have significant effects on tropospheric weather and climate. However, in the past ~5-10 years, the prevailing view has changed, and variability in the extra-tropical atmospheric flow is now recognised to reflect "two-way" interactions between the stratospheric and tropospheric circulations.

The relationship between the stratospheric and tropospheric circulations is most clearly evident as deep vertical coupling in the "annular modes" of extra-tropical climate variability (Thompson and Wallace, 1998; Thompson and Wallace, 2000). The annular modes extend from the surface through the stratosphere in both hemispheres, and are characterized by meridional vacillations in the geopotential height field between the polar regions and surrounding middle latitudes. Fluctuations in the annular mode index at a given pressure level are nearly equivalent to fluctuations in the geopotential anomaly averaged over the po-

lar cap (Baldwin and Thompson, 2009). During the cold season in the stratosphere, the annular modes correspond to fluctuations in the strength of the polar vortex, while at the surface the annular modes correspond to meridional shifts in the extra-tropical storm tracks. The stratospheric and tropospheric components of the annular modes are coupled in both hemispheres, particularly in winter in the Northern Hemisphere (NH), and in spring in the Southern Hemisphere (SH), but the reasons for this coupling are still not understood.

Stratosphere-troposphere coupling is also an important process in the context of climate change. Any long-term changes in stratospheric winds and temperatures are likely to affect surface climate and climate variability. During the past ~25 years, the composition of the stratosphere has changed substantially. Abundances of anthropogenic greenhouse gases (GHGs) and ozone-depleting substances (ODSs) have risen, while stratospheric ozone has been depleted, particularly in the Antarctic vortex. Following the successful implementation of the Montreal Protocol and its ammendments, the concentrations of ozone-depleting substances in the stratosphere have stabilized, and the severity of the ozone hole is expected to decrease over the coming decades. However, concentrations of most greenhouse gases will continue to rise. It is therefore necessary to view stratosphere-troposphere coupling in the context of a changing atmosphere.

It has long been known that radiative processes are important for stratosphere-troposphere coupling in the context of climate change. For example, stratospheric cooling induced by CO_2 increases has long been known to offset part of the induced tropospheric warming, and radiative forcing at the tropopause is routinely reported after allowing for the radiative influence of altered stratospheric temperatures (WMO, 1992; Forster *et al*., 2007). Similarly, stratospheric ozone depletion is thought to exert a small cooling influence on the troposphere in the global mean, while increases in stratospheric water vapour have caused a warming effect at the surface (Forster *et al*., 2007). Moreover the effect of stratospheric volcanic aerosol on tropospheric climate is primarily radiative, and exerts a substantial influence on the global radiative budget on a time scale of ~2 years. The radiative forcing immediately following Pinatubo is estimated to be -3 W m^{-2} in the global mean (Forster *et al*., 2007). Recently, interest in the radiative response to stratospheric forcings has moved beyond the global mean, and several recent studies have examined the role of radiation in driving the regional pattern of temperature response to stratospheric ozone depletion. Early work using radiative-convective models already suggested that Antarctic ozone depletion could force substantial local surface cooling, as observed (Lal *et al*., 1987). More recent work confirms that cooling of the Antarctic troposphere in late spring and summer is likely largely a radiative re-

Table 10.1: Key diagnostics

Process	Diagnostic	Variables	Data, Models	References[a]
Climate				
Mean Climate	u mean, variability	u	NCEP, ERA-40	
	Combined Performance metrics	u, v, T	NCEP, ERA-40, CMIP3, CCMVal-1	*Reichler and Kim (2008)*
Climate Trends	Linear trends, 20th Century	T, Z, O_3	CMIP3	*Thompson and Solomon (2002)*
	Long-term change REF-B2	u, T, O_3, jet, Hadley cell	CMIP3	*Thompson and Solomon (2002)*
Dynamical Coupling[b]				
NAM, SAM	Annular Modes	Z	ERA-40, NCEP	*Thompson and Baldwin (2009)*
	AM RMS amplitude	Z	ERA-40, NCEP	*Gerber et al. (2010)*
	Latitude of AM node	Z	ERA-40, NCEP	*Gerber et al. (2010)*
	Seasonal AM variance	Z	ERA-40	*Baldwin et al. (2003)*
	Tropospheric AM predictability	Z	ERA-40	*Baldwin et al. (2003)*
	AM e-folding time scale	Z	ERA-40	*Baldwin et al. (2003)*
Radiation				
Radiative Forcing	Ozone-induced radiative forcing	O_3		*Forster et al. (2007)*
Erythemal Irradiance	Surface erythemal irradiance	O_3, T		*Mayer and Kylling (2005)*
Ozone Fluxes				
	Ozone flux from stratosphere	$O_3, \overline{w}^*$	ERA-Interim	*Hegglin and Shepherd (2009)*

[a] *Listed references only provide examples*
[b] *Abbreviations: AM=Annular Mode*

sponse to ozone-induced stratospheric cooling (Keeley *et al*., 2007; Grise *et al*., 2009). Radiative processes may also play a role in intra-seasonal coupling between the stratosphere and troposphere (Ramanathan, 1977; Grise *et al*., 2009).

The stratosphere also influences the troposphere through the exchange of radiatively active gases across the tropopause. The most important such influence is on tropospheric ozone, the third largest contributor to greenhouse-gas-induced radiative forcing after CO_2 and methane. While the flux of ozone from the stratosphere is only about 10% as large as the tropospheric chemical production source, it delivers ozone directly to the upper troposphere, where its effect on radiative forcing is largest (Denman *et al*., 2007, Table 7.8; Stevenson *et al*., 2006). Climate change simulations with models including tropospheric chemistry indicate that an increase in stratosphere-troposphere exchange is a dominant driver of changes in tropospheric ozone (Stevenson *et al*., 2006).

The recent projections of climate change considered by the IPCC (IPCC, 2007), which focus on the troposphere, are mainly based on the Coupled Model Intercomparison Project phase 3 (CMIP3) climate models, which have varying vertical resolution in the stratosphere. These models generally do not have substantial interactive chemistry, and they are not designed to predict changes to the ozone layer or the dynamics of stratosphere/troposphere coupling. Further many of the models contain constant ozone concentrations, and those which do represent ozone depletion generally specify zonal-mean ozone concentrations, which may make the climate response to specified ozone changes unrealistic (Crook *et al*., 2008; Waugh *et al*., 2009). The CCMVal models include good representations of the stratosphere and interactive ozone chemistry, and can therefore simulate changes to the ozone layer and coupling to climate change, though SSTs are in general specified, thereby constraining the surface climate response. In this chapter we use the CMIP3 models as a baseline against which to

Table 10.2: Models used for model validation.

	monthly (mean and interannual variability)	daily (synoptic variability)
CMIP3 (20C3M, AMIP)	CNRM_CM3, GFDL_CM2_1, GISS_MODEL_E_R, INMCM3_0, IPSL_CM4, MIROC3_2_HIRES, MIROC3_2_MEDRES, MPI_ECHAM5, MRI_CGCM2_3_2A, NCAR_CCSM3_0, NCAR_PCM1, UKMO_HADGEM1	CNRM_CM3, GFDL_CM2_1, GISS_MODEL_E_R, INMCM3_0, MIROC3_2_HIRES, MIROC3_2_MEDRES, MPI_ECHAM5, MRI_CGCM2_3_2A
CCMVal-1 (REF-1)	AMTRAC, CCSRNIES, CMAM, E39C, GEOSCCM, LMDZREPRO, MAECHAM4CHEM, MRI, SOCOL, ULAQ, UMETRAC, UMSLIMCAT, WACCM	
CCMVal-2 (REF-B1)	AMTRAC3, CAM3.5, CCSRNIES, CMAM, CNRM-ACM, E39CA, EMAC, GEOSCCM, LMDZrepro, MRI, NiwaSOCOL, SOCOL, ULAQ, UMSLIMCAT, UMUKCA-METO, UMUKCA-UCAM, WACCM	AMTRAC3, CCSRNIES, GEOSCCM, LMDZrepro, SOCOL, UMUKCA-METO, WACCM
CCMVal-2 QBO	CAM3.5, CCSRNIES, E39CA, EMAC, MRI, NiwaSOCOL, SOCOL, ULAQ, UMSLIMCAT, UMUKCA-METO, UMUKCA-UCAM, WACCM	CCSRNIES, SOCOL, UMUKCA-METO, WACCM

compare the CCMVal models: This allows us to assess the impacts on stratosphere-troposphere coupling of a better-resolved stratosphere and stratospheric processes.

In this chapter we will review stratosphere-troposphere coupling in the CCMVal models, and compare CCMVal simulations with observations and other models, such as the CMIP3 models. We will investigate what is required to realistically simulate stratosphere-troposphere coupling in climate models.

10.2 Validation of tropospheric and stratospheric climate

In this section we compare measures of mean climate and variability in the stratosphere and troposphere of the CCMVal-2 models with observations. Coupled chemistry-climate models generally have higher stratospheric resolution and more realistic stratospheric processes than conventional climate models, suggesting that their representation of stratospheric climate may be better. Given the notion that the stratosphere and the troposphere form a two-way interacting system, one might even argue that an improved stratosphere should lead to a superior troposphere. On the other hand, less attention is typically devoted to a realistic simulation of the troposphere when developing coupled chemistry-climate models (CCMs). In order to assess which of these different viewpoints is most appropriate, this subsection will use broad aspects of mean climate and climate variability to evaluate CCMVal-2 and other classes of climate models. The performance metric used here is based on zonal mean quantities describing the large-scale circulation and the temperature structure of the atmosphere.

Table 10.2 gives an overview of model output considered in this comparison. All available model output from the CCMVal-2 simulations is employed. In addition, results from CMIP3 (Meehl *et al*., 2007a) and the "First Chemistry-Climate Model Validation (CCMVal-1) (Eyring *et al*., 2007) are included. The CMIP3 data set contains simulations from all the major coupled ocean-atmosphere models around the world, compiled around 2005. The corresponding models were not specifically designed to resolve the stratosphere, and their stratospheric resolution, which varies greatly from model to model, is generally lower than that of the CCMVal-2 models. Thus, comparing CMIP3 with CCMVal should shed some light on the effects of a well-resolved stratosphere on the simulation of tropospheric climate.

The exact number of models examined depends on the type of analysis. Analysis based on monthly means includes 12 models from CMIP3, 13 models from CCMVal-1 (REF-1 experiment), and 18 models from CCMVal-2 (REF-B1 experiment). Some models provided multiple ensemble members; in this case all available members are used and appropriately combined into a mean outcome. Analysis of daily data is limited to fewer models because the necessary output was not provided by all models. The ERA-40 rean-

alysis (ERA-40, Uppala *et al.*, 2005) is used as a reference against which the simulations are validated. The NCEP/NCAR reanalysis (NNR) is also used to provide an indication of uncertainty associated with the reanalysis method.

The performance metric used in this comparison is based on zonal means of zonal wind (*u*), meridional wind (*v*), and temperature (*T*). Clearly, it would have been desirable to include more than three quantities, but this was not possible because of the limited amount of archived model output. The above three quantities are examined from pole to pole and from the surface to the mid-stratosphere. In most of the analysis tropospheric (1000 - 200 hPa) and stratospheric (150 - 10 hPa) climate is investigated separately. The common base period for models and observations is 1979-1999, and three different categories of climate are investigated: (1) long-term means, (2) interannual variability, and (3) synoptic variability. Interannual variability is calculated from seasonal mean anomalies over the given number of years. Synoptic variability is calculated from daily high-pass filtered anomalies, derived by removing a low-pass filtered version of the daily data (using a Gaussian weighting with a "full width at half maximum" of 15 days) from the original daily data. Multi-model variability is computed by concatenating the anomaly time series from all participating models (including all ensemble members) and then calculating variability. Before errors are calculated all model data are interpolated to the common grid of the validating ERA-40 reanalysis.

For each climate category and climate quantity two different measures of error are considered: First, the pattern correlation (*r*) between the simulated and observed spatial fields, and second, the normalised error variance (*E²*) or root mean square error (*E*). *E²* is defined by

$$E^2 = \sum_{n=1}^{N} w_n d_n^2 , \qquad (10.1)$$

where w_n indicates appropriate weighting by the cosine of latitude, the layer thickness in log pressure (corresponding approximately to weighting each grid cell by its volume), and the number *N* of grid points, and d_n represents a (normalised) difference between simulated and observed fields at grid point *n*. For the analysis of mean climate, d_n is taken to be the difference between model and observations, normalised by the observed local interannual standard deviation. This can be written as

$$d_n = \frac{m_n - o_n}{\sigma_{n,o,\text{inter}}} , \qquad (10.2)$$

where *m* and *o* represent the mean climate of model and observations, and σ denotes the observed interannual standard deviation (Reichler and Kim, 2008). For the analysis of climate variability, d_n represents the $\log_2$ variability ratio between model and observations, or

$$d_n = \log_2 \frac{m_n}{o_n} . \qquad (10.3)$$

Here, *m* and *o* are the standard deviations on interannual or synoptic time scales. With this definition, a perfect simulation has a variability ratio of zero, and positive or negative values indicate the factor by which a model over- or underestimates the observed variability. The above two definitions for *d* result in normalised and non-dimensional error estimates that can be compared across quantities.

In some of the analysis, the individual *r* and *E²* values for the different quantities and/or models are combined into an overall error estimate. This is accomplished by taking simple averages of the *E²* values. The correlations *r*, however, are combined by averaging their Fisher-z-transformed values and by applying the inverse Fisher-z-transform to the average.

The error calculations are carried out separately by quantity (*u, v, T*), season (January-March, JFM; October-December, OND), model, and also for the multi-model mean. The analysis is focused on the northern extra-tropics (30°N-90°N) during JFM and the southern extra-tropics (30°S-90°S) during OND. These two cases were chosen because they represent the time when and the region where the dynamical coupling between the stratosphere and troposphere is expected to be strongest (Baldwin *et al.*, 2003). One should therefore expect that the possibility that the simulations of the stratosphere and the troposphere are related is maximised.

10.2.1 Multi-model mean comparison

The zonal mean cross sections in **Figure 10.1** present multi-model mean errors for zonal wind during JFM for mean climate and its interannual variability. The errors shown are simple differences (*i.e.*, $\overline{m}_k - o_k$ or $\log_2(\overline{m}_k/o_k)$) between the multi-model means ($\overline{m}$) and ERA-40.

Overall, the outcomes from the two CMIP3 experiments (20C3M and AMIP) are very similar, indicating that specifying observed SSTs has only a limited impact on the simulation of zonal winds. For mean climate, both CMIP3 experiments exhibit a pronounced positive wind bias extending down from the stratosphere into the troposphere. This leads to tropospheric jets that are too strong over the NH and equatorward and upward shifted over the SH. The error patterns in interannual variability show large negative biases in the tropical stratosphere. This lack of variability is because most CMIP3 models do not simulate the Quasi-Biennial Oscillation (QBO). The CMIP3 models as a group also have a tendency toward too much variability over the SH extra-tropics.

The multi-model mean simulations of CCMVal-1 and CCMVal-2 are also quite similar, although biases tend to be somewhat smaller in the more recent CCMVal-2 models. Comparing CCMVal models against CMIP3 models provides clear evidence that, overall, the stratosphere-resolving CCMVal models perform better in their simulations
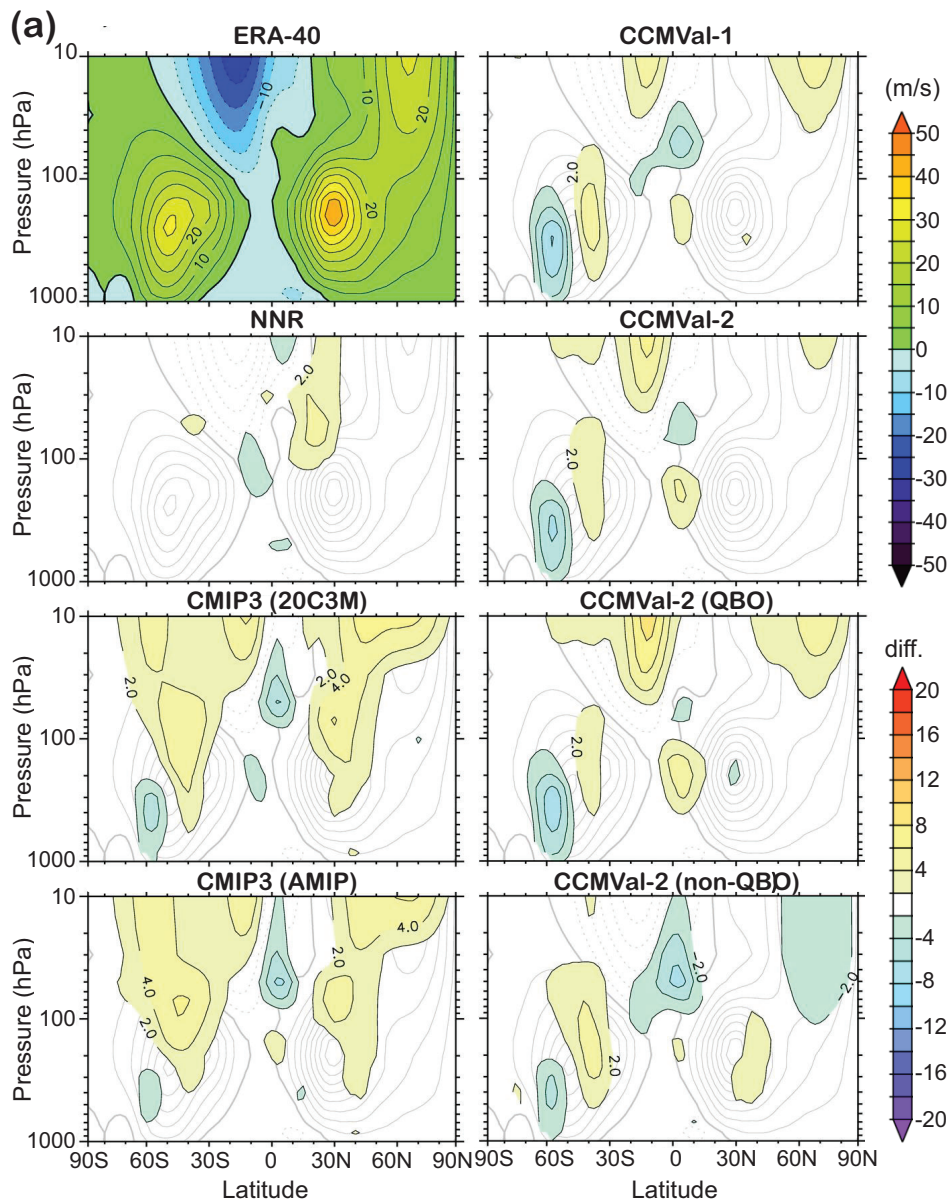
Figure 10.1: JFM multi-model errors in zonal-mean zonal wind. Errors are based on (a) mean climate and (b) interannual variability. The first panels show full fields (in m/s) from the validating ERA-40 reanalysis. The remaining panels show errors for the NCEP/NCAR reanalysis and for the various multi-model groups. Yellowish (bluish) colours indicate positive (negative) errors. Errors in (a) mean climate are differences drawn at 2 m/s intervals. Errors in (b) variability are $\log_2$-variability ratios drawn at 0.5 contour intervals. Grey contour lines indicate full fields from the validating ERA-40, shown in the first panels.

of mean stratospheric circulation. The CCMVal models also exhibit more realistic variability in the tropical stratosphere, even in those models without a QBO, although the CCMVal-2 models tend to exhibit a larger high bias in JFM SH stratosphere variability than the CMIP3 models, very likely associated with the delayed SH final warming seen in these models (Section 4.4.4). In the troposphere, the general problem of a shifted southern hemispheric jet is even more pronounced in the CCMVal models. In addition, the

CCMVal models exhibit an even larger bias in interannual variability in the SH troposphere than the CMIP3 models. It also seems that the tropospheric wind simulations are somewhat more realistic in CMIP3, but the differences are quite subtle. This could be because more attention is focused on tuning the CMIP3 models to reproduce a realistic tropospheric climate than for the CCMVal-2 models.

Stratifying CCMVal-2 into QBO-producing and non-QBO-producing models shows the expected impact on the
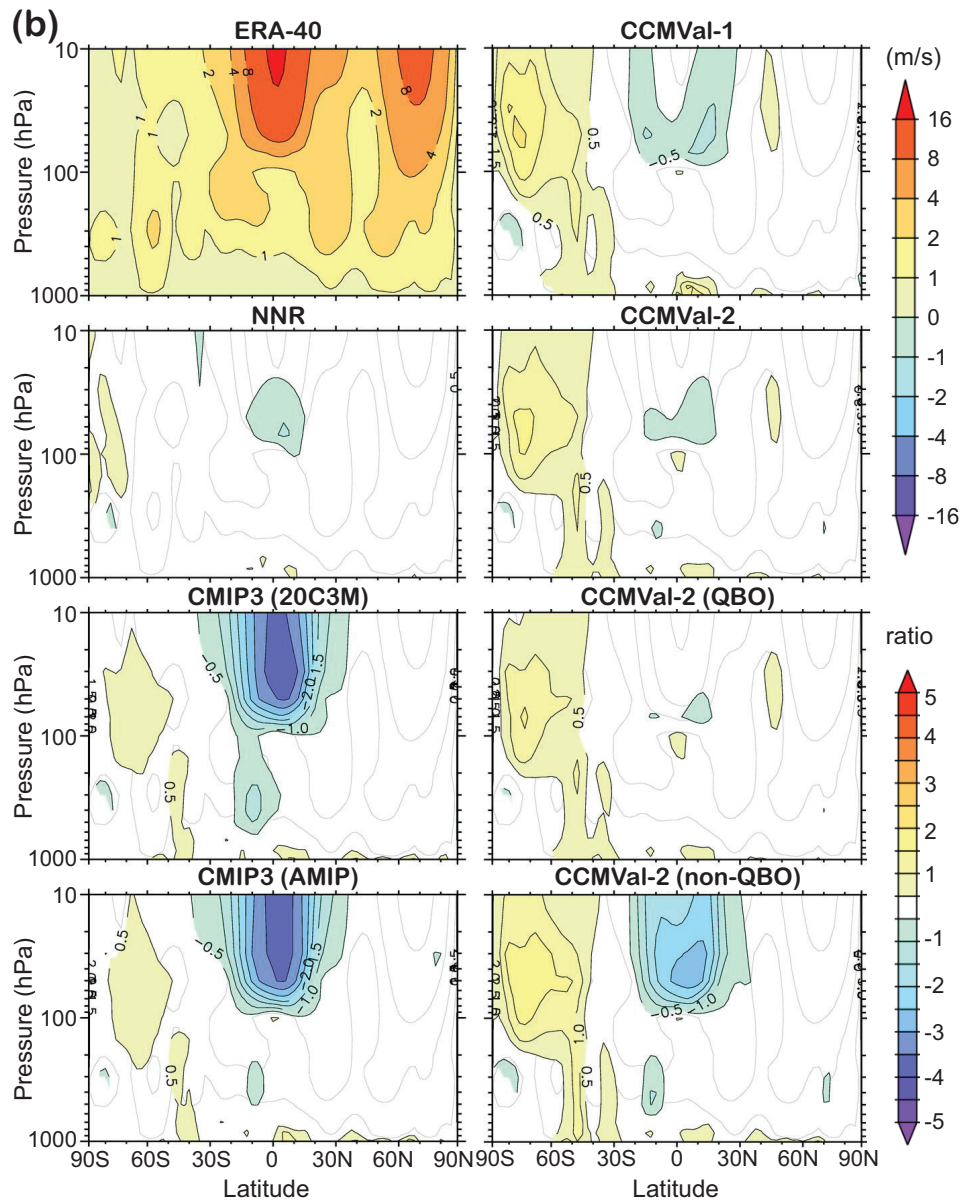
(b)

Figure 10.1 continued.

interannual variability in the tropical stratosphere. This, however, does not seem to affect the extra-tropical interannual variability much, and the problem of a positive bias in variability over the SH exists in both model groups.

10.2.2 CCMVal-2 performance

The diagrams in **Figure 10.2** summarize the combined errors in zonal and meridional wind and temperature for the individual CCMVal-2 models. The *x* and *y* axes show the normalised root mean square errors *E*, and the pattern correlations *r*, such that the best performing models are located in the lower left corner. The grey contour lines combine *r* and *E* into a single skill index *S* according to

$$S = \frac{r^2}{1 + bE^2}, \qquad (10.4)$$

where the parameter *b* assigns a relative weight to the two error components *r* and *E*. Here, *b* is chosen such that *S* = 1% if *r* = 1 and *E* = 30.

Individual models are identified by the first two letters of their official model names (Table 10.2). The larger filled "2" symbols indicate the median of all models. Colour is used to discriminate six different aspects of model performance, hue indicates tropospheric (reddish) and stratospheric (bluish) performance, and colour intensity indicates performance for the three climate categories, *i.e.*,
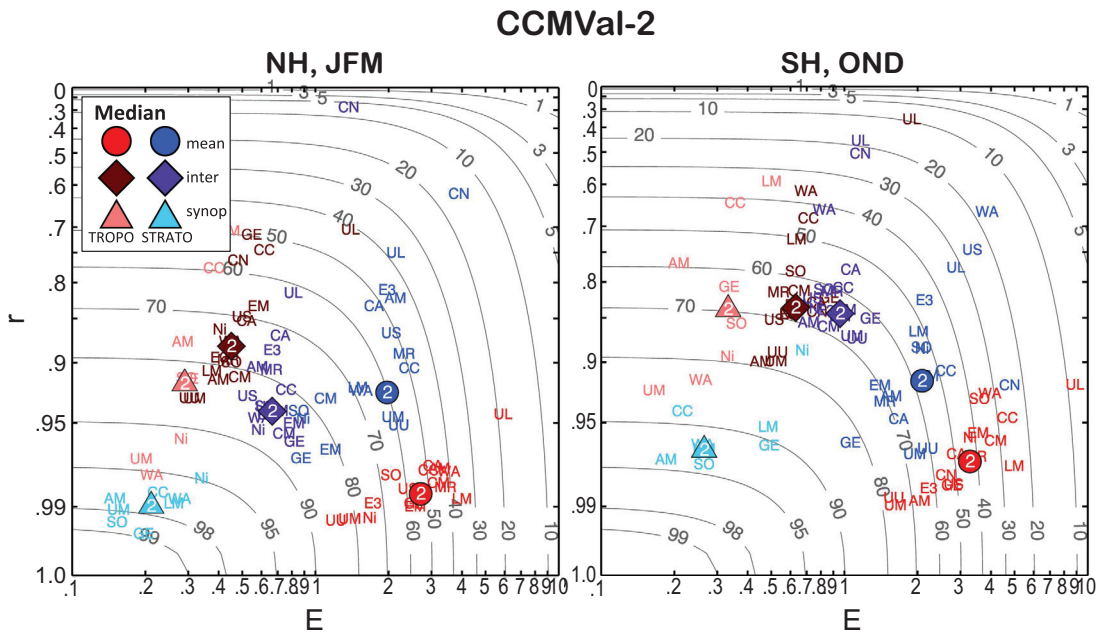
CCMVal-2

Figure 10.2: CCMVal-2 seasonal mean combined performance for *u*, *v*, and *T*. Performance is shown in terms of (y-axis) pattern correlation, (x-axis) normalised RMS error, and (gray contours) skill S (in %). Lower left (upper right) corner corresponds to best (worst) performance. Left panel is for NH (30°N-90°N) (January-March) and right panel is for SH (30°S-90°S) (October-December) extra-tropics. Blue (red) colours indicate stratospheric (tropospheric) performance. Colour intensity indicates: (light) synoptic variability; (dark) interannual variability; (medium) mean climate. Individual models are identified by first two letters of their official model names. US, UM, and UU denote UMSLIMCAT, UMUKCA-METO, and UMUKCA-UCAM, respectively. Large filled symbols denote the median outcome of all models in one group.
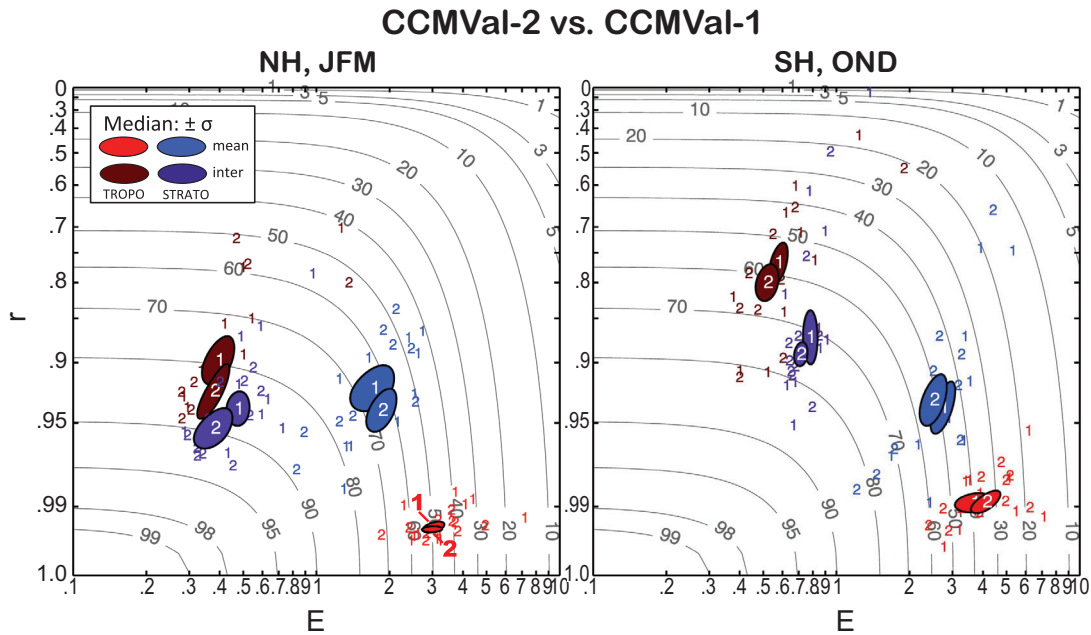
CCMVal-2 vs. CCMVal-1

Figure 10.3: Comparison between CCMVal-2 and CCMVal-1 for u and T. Individual models are indicated by "1"s (CCMVal-1) and "2"s (CCMVal-2). Oval shapes indicate ±1σ uncertainty ranges of median performance for each model group. The shapes are ellipses that are distorted by the logarithmic scale of the axis. See the caption to Figure 10.2 for more details.

mean (medium), interannual variability (dark), and synoptic variability (light). Thus, each model's performance, and the multi-model means appear six times on each diagram.

The outcomes for the different climate categories tend to be well separated from each other. For example, stratospheric skill is generally higher than tropospheric skill, mean climate is usually associated with larger r and E values and interannual variability with smaller ones. Within each performance category, the variation of E and r leads to elongated structures of individual model outcomes. Models also tend to perform better over the NH during JFM (left) than over the SH during OND (right), which is in part related to the fact that the two diagrams represent different seasons (boreal winter and austral spring). However, taking all seasons together skill values are still generally higher over the NH than over the SH (not shown),

As indicated by the median outcomes ("2" symbols), overall the models match the observations quite well. In most cases, the pattern correlations exceed 70% and the root mean square errors amount to less than four standard deviations. This leads to skill scores of 50-70%. However, there are also some noticeable outliers. ULAQ underperforms in all categories of climate: in stratosphere and troposphere, over both hemispheres, and in mean climate as well as in interannual variability. CNRM-ACM performs well in the troposphere but underperforms in the stratosphere, which is likely related to the strongly equatorward displaced jet in this model (Figure 4.3). WACCM performs poorly in the SH, which is likely related to a strong late bias in the final warming date for this model (Figure 4.27). In summary, these results suggest that there is a wide range of performances amongst the individual CCMVal-2 models, with some models clearly being identifiable as outliers.

As explained before, the model results represent means of all available ensemble members. However, outcomes for individual realizations for models that provide multiple members are very similar ($\Delta S < 5\%$, not shown), indicating that the results are robust. For clarity, the outcomes of validating NNR against ERA-40 are also omitted. However, the skill of NNR generally ranges between 80 and 99% and thus exceeds that of any individual model.

10.2.3 CCMVal-2 vs. CCMVal-1

CCMVal-2 is a continuation of the former CCMVal-1 project, and it is natural to ask whether the new features and improvements implemented in CCMVal-2 models also translate into better climate simulations. This issue is addressed in **Figure 10.3**. The diagrams here are similar to Figure 10.2 except that synoptic variability is omitted and that errors in meridional wind are not considered (both because of limited data from CCMVal-1). Another difference is that median outcomes are replaced by median uncertainty estimates. These estimates were derived by bootstrap-

ping, *i.e.*, by randomly selecting the models included in the calculation of the median and by repeating this procedure many (1000) times. The resulting probability distributions were used to determine the $\pm 1\sigma$ median intervals, which are shown by the filled oval structures.

Figure 10.3 only includes models that participated in both the CCMVal-1 and the CCMVal-2 activity. Individual model outcomes are indicated by "1" and "2" for CCMVal-1 and CCMVal-2, respectively. In most cases there is overlap between the median uncertainty estimates of the two model groups, indicating that the performance differences between CCMVal-1 and CCMVal-2 are small. In particular, CCMVal-1 and CCMVal-2 produce tropospheric mean climate simulations (medium red) that are almost identical. In the other climate categories, however, CCMVal-2 tends to have somewhat higher skill, indicating slight, but non-significant, improvements of CCMVal-2 over its first generation predecessor.

10.2.4 CCMVal-2 vs. CMIP3

Figure 10.4 presents a comparison between CCMVal-2 and CMIP3. The average over all three climate quantities is displayed. In order to make the comparison fair, CMIP3 model output was derived from the AMIP-type experiment, meaning that both CCMVal-2 and CMIP3 models were forced with prescribed sea surface temperatures (SSTs) and sea ice.

From the median uncertainty estimates one can see that tropospheric mean climate and tropospheric synoptic variability are simulated quite similarly by the two model groups. In the other categories, however, CCMVal-2 generally outperforms CMIP3. This is perhaps to be expected in the stratosphere, but interannual variability in the troposphere over both hemispheres is also better simulated in CCMVal-2. We investigated whether this result is related to the simulation of a more realistic QBO by many CCMVal-2 models. However, stratifying CCMVal-2 into QBO and non-QBO producing models (not shown) does not support this hypothesis. These results provide clear evidence that the improved representation of stratospheric processes in the CCMVal-2 models gives an improved stratospheric climate relative to the CMIP3 models. Moreover, this improvement is not realized at the expense of tropospheric simulation quality.
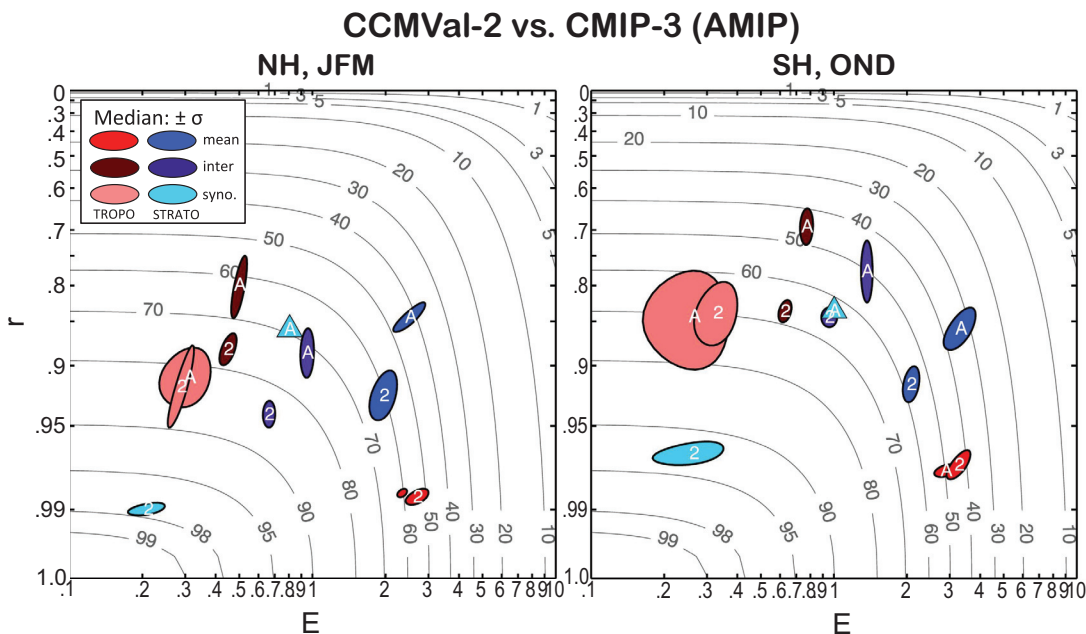
CCMVal-2 vs. CMIP-3 (AMIP)

Figure 10.4: Median uncertainty comparison between CCMVal-2 (REF-B1) ("2") and CMIP3 (AMIP experiment) ("A") for u, v, and T combined. For clarity, individual model outcomes are not shown. For CMIP3, daily variability in the stratosphere is only based on the GFDL_CM2.1 model and thus the median estimate is replaced by a light blue triangle. See caption Figure 10.3 for additional information.

10.3 Evaluation of Stratosphere-Troposphere Coupling in Models

10.3.1 Downward propagation of Annular Mode anomalies

Baldwin and Dunkerton (1999, 2001) demonstrated that circulation anomalies originating in the stratosphere propagate downwards and influence the tropospheric circulation for up to two months. In this subsection the downward propagation of circulation anomalies in the CCMVal-2 models is examined using time series of the annular mode indices. The Northern Annular Mode (NAM) and Southern Annular Mode (SAM) at each pressure level are defined here as the first Empirical Orthogonal Functions (EOFs) of the daily zonal-mean geopotential height between the equator and the respective pole, weighted by the square root of the cosine of latitude. Before the analysis, the global-mean geopotential height is removed each day and a slowly-varying seasonal climatology is also removed (Gerber *et al.*, 2010). The annular mode indices are computed by projecting the area-weighted daily geopotential height anomalies onto the EOF patterns, and are normalised to have unit variance. For the model integrations, the annular modes were calculated from one realization of the REF-B1 scenario. The indices from all integrations of a given model were then computed by projecting

the detrended geopotential height anomalies onto this pattern. As the annular mode statistics appear to be relatively insensitive to climate trends, we use all REF-B0, -B1, and -B2 scenario integrations available to maximise the sample size. ECMWF and NCEP-NCAR reanalyses were analysed from 1958–2008 in the NH and 1979–2008 in the SH, due to the poor quality of the reanalyses prior to the advent of satellite observations in the SH.

Daily mean (or instantaneous) fields are provided by nine CCMVal-2 models (REF-B1 simulations). For those models which provided multiple realizations the time series were constructed by concatenation of all available realisations. We also use output from BCCR-BCM2.0, GFDL CM2.0 and GFDL CM2.1, the only CMIP3 models that provide daily geopotential height data. These are low top models with upper layers at 10 hPa, 3 hPa and 3 hPa respectively. Following Baldwin and Dunkerton (2001) and Thompson *et al.* (2005), we show composite differences of strong and weak stratospheric annular mode events. The strong (weak) events are determined by the dates on which the 10-hPa NAM index cross the ±2 standard deviation threshold. Only one event per year (the one with the largest magnitude) is chosen because the time scale of the events is comparable to the length of the dynamically active season.

Figure 10.5 shows a comparison of composite differences of the NAM index for ERA-40 data and ten models. The models capture the downward propagation of NAM
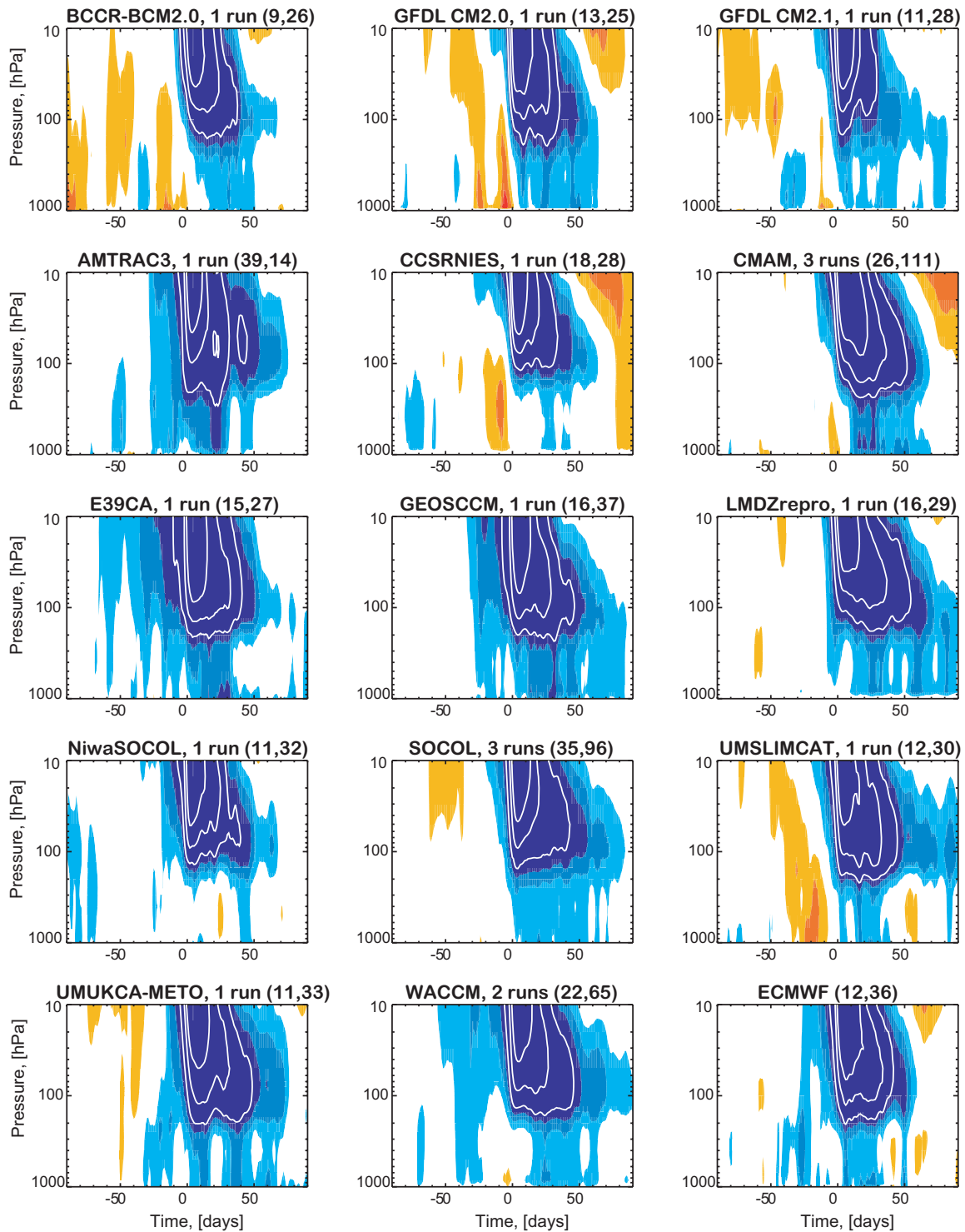
Figure 10.5: Composite differences of the standardized NAM index between strong and weak stratospheric vortex events. Results are shown for three CMIP3 models for which suitable daily data were available (top row), eleven CCMVal-2 models (REF-B1 simulations) with daily data available, and the ERA-40 reanalysis. Day 0 corresponds to the onset of the stratospheric event at 10 hPa. The shading interval is at 0.5 standard deviations and the contour interval is 1 standard deviation. Shading is drawn for values exceeding 0.5 standard deviations. Blue shading denotes positive values in the NAM index. Numbers above each panel indicate numbers of strong and weak events included in the composite.
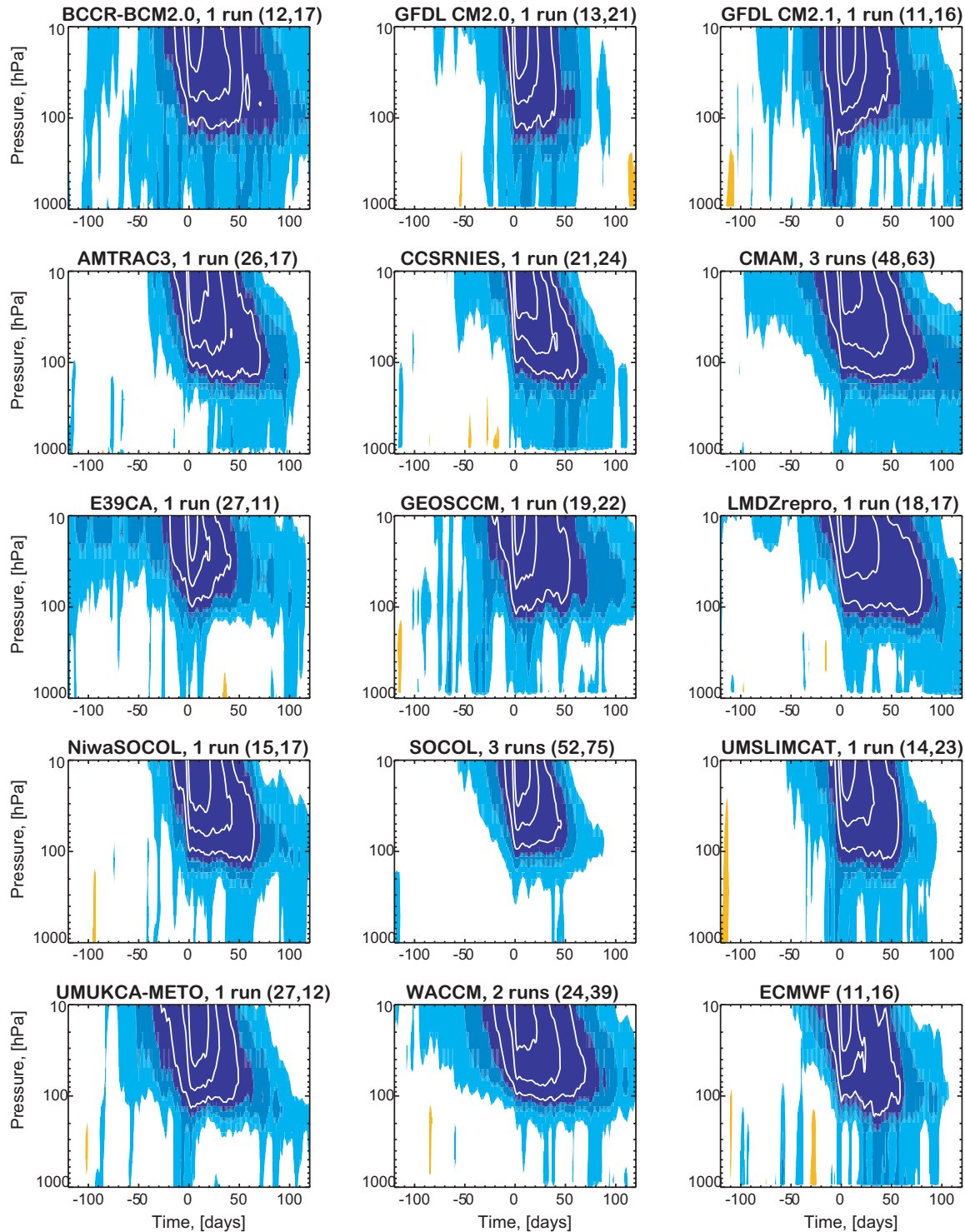
Figure 10.6: Composite differences of the standardized SAM index between strong and weak stratospheric vortex events. Results are shown for three CMIP3 models for which suitable daily data were available (top row), eleven CCMVal-2 models (REF-B1 simulations) with daily data available, and the ERA-40 reanlaysis. Day 0 corresponds to the onset of the stratospheric event at 10 hPa. The shading interval is 0.5 standard deviations and the contour interval is 1 standard deviation. Shading is drawn for values exceeding 0.5 standard deviations. Blue shading denotes positive values in the SAM index. Numbers above each panel indicate numbers of strong and weak events included in the composite, and are lower for ERA-40 because observations were taken solely from the period 1979-2008.
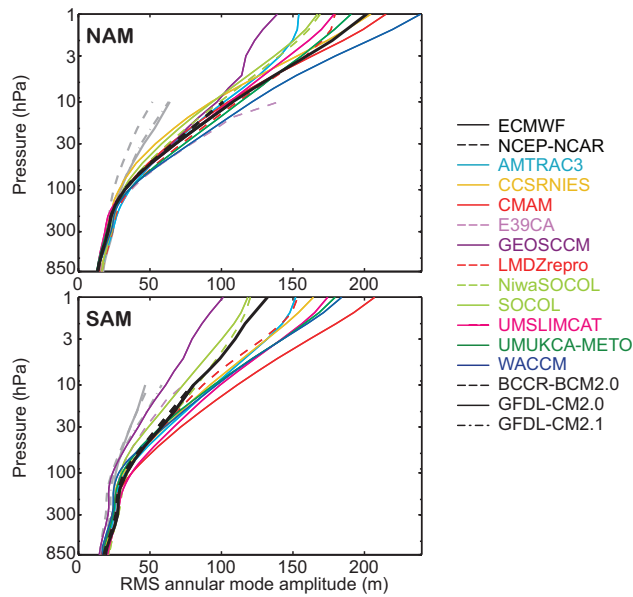
Figure 10.7: The RMS amplitude of the annular mode pattern of variability as a function of pressure in the (top) NH and (bottom) SH. Analysis of three CMIP3 models (gray lines) are included for reference.

anomalies, including the low-top CMIP3 models. Given the relatively short (50 year) observational period and model runs, there is a lot of sampling noise in the troposphere, and no significance can be attached to the short-period variations in the troposphere. However, a comparison of similar plots based on multiple ensemble members from one model (not shown) indicates that inter-model differences are in most cases larger than differences between ensemble members from the same model. All models show that large anomalies tend to extend downward to near the tropopause, as in the observations. In some models (most clearly in GEOSCCM and LMDZrepro), the anomalies in the lower stratosphere and troposphere tend to last too long compared with observations (see also Section 10.3.2). **Figure 10.6** shows composite differences of the SAM index between strong and weak SAM events. After the peak at 10 hPa, the anomalies descend to the lower stratosphere in both ERA-40 and the models. In ERA-40, the tropospheric anomalies peak 30-40 days after the onset of the event at 10 hPa, with values exceeding 1.5 standard deviations, and persist for at least three months after the onset. All the models reproduce tropospheric anomalies following the stratospheric events. As in the NH, some models (BCCR-BCM2.0, CMAM, GEOSCCM, and LMDZrepro) show noticeably longer persistence of the anomalies in the lower stratosphere compared with the observations.

10.3.2 Annular mode time scales and predictability

We first quantify the amplitude of the annular mode (AM) variability as a function of height in **Figure 10.7**. All CCMVal-2 models simulate the amplitude of the annular modes in the stratosphere more accurately than the three CMIP3 models for which upper atmospheric output is available. The improvements are particularly evident in the NH. Nearly all CCMVal-2 models correctly capture the increased variance of the NAM relative to the SAM. There is substantially more spread between the models and reanalyses in the SH, suggesting less agreement between models in representing SH dynamics. This is consistent with differences in the temporal variability, as documented below.

Figure 10.8 compares the seasonal and vertical structure of the annular mode variance in the ECMWF reanalysis and the multi-model ensemble mean. The models, both as a group and individually (not shown), simulate the structure quite well, capturing the marked asymmetry of the AM seasonal cycle between the two hemispheres. The seasonal cycle in models, however, is slightly delayed in both hemispheres, particular in the lower stratosphere. This is likely a consequence of a delayed break down of the vortex, and, in the NH, of limited variability in the early winter (see Figure 4.27).

The models capture the qualitative structure of the annular mode temporal variability, as seen in the seasonal and vertical evolution of the AM *e*-folding time scale in **Figure 10.9**. This time scale is found by computing a seasonally localized autocorrelation function at each pressure level and calendar date, which is then fit to an exponential function (Baldwin *et al.*, 2003). It thus provides a rough estimate of the persistence of AM anomalies. It is important to interpret these time scales in the context of the variance structure shown in Figure 10.8. The time scales are most meaningful when the AM is active; the extreme persistence in the NH summer, for instance, occurs during a period when there is almost no variability of the NAM, and could be due to very small variations in total column ozone left over from the previous winter (Fioletov and Shepherd, 2003). The models simulate the NH-SH asymmetry in the seasonal cycle of the AM *e*-folding time scale, both in the troposphere and lower stratosphere, and the tendency towards longer time scales in the SH. The models, however, overestimate the time scales, particular in the SH (note the nonlinearity of the colour scale). The biases in the troposphere are similar to those found in the CMIP3 models (Gerber *et al.*, 2008). In addition, the seasonal cycle of the time scales is delayed and broadened in both hemispheres.

Comparison between Figures 10.8 and 10.9 suggests a close relationship between increased *variance* of the AM in the lower stratosphere and increased *persistence* of the
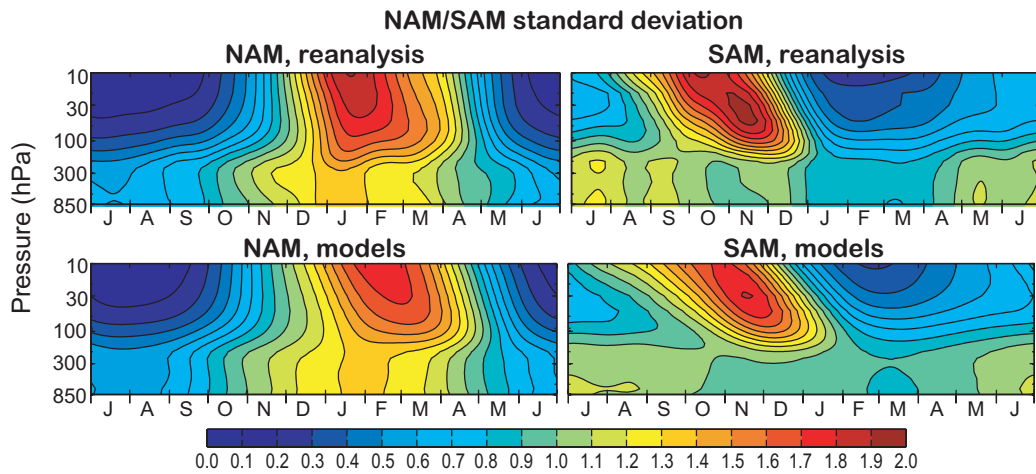
Figure 10.8: The variance of the NAM and SAM indices as a function of season and height: (top) ECMWF reanalysis and (bottom) the multi-model ensemble mean. Note that the indices have been normalised to have unit variance at all levels, removing the systematic increase in variance with height shown in Figure 10.7.
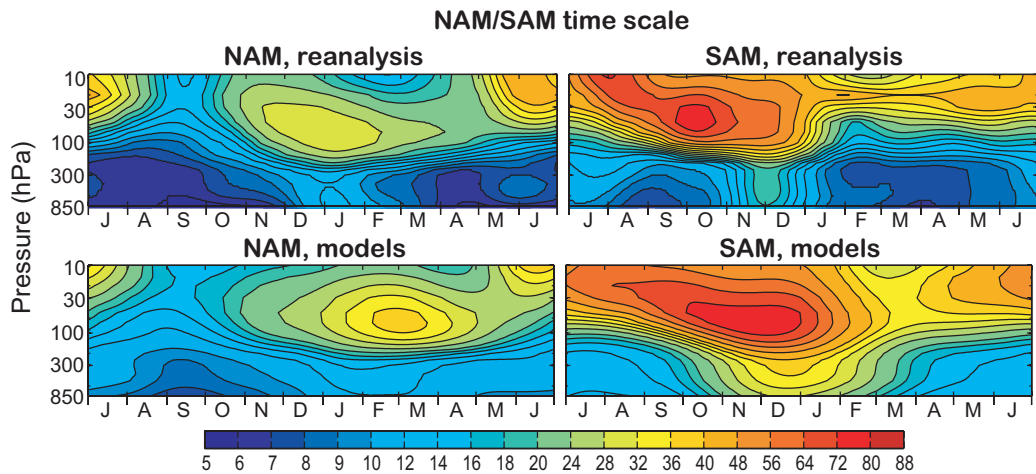

Figure 10.9: The e-folding time scale of the NAM and SAM indices as a function of season and height: (top) ECMWF reanalysis and (bottom) the multi-model ensemble mean.
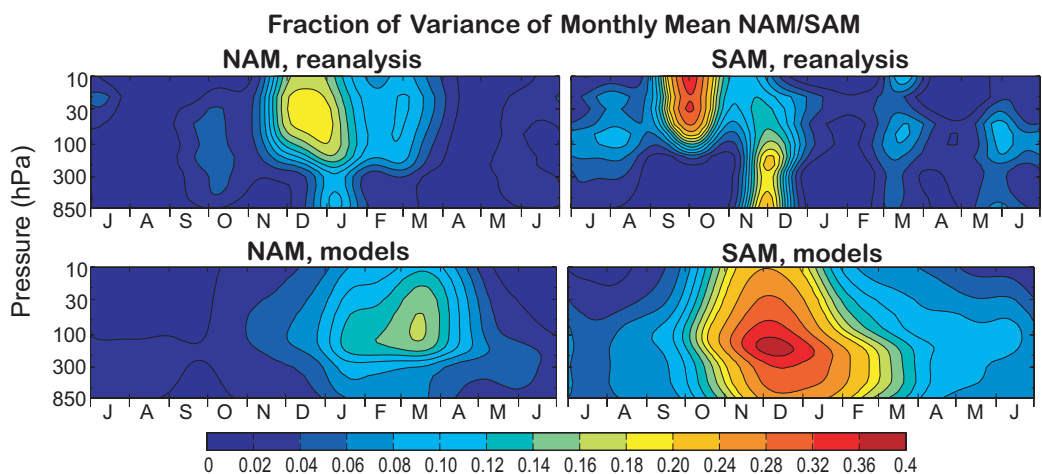

Figure 10.10: The fraction of the variance of the monthly mean 850 hPa AM index, lagged by 10 days, that is linearly correlated with the instantaneous AM index as a function of season and height: (top) ECMWF reanalysis and (bottom) the multi-model ensemble mean.

AM in the troposphere in both the reanalysis (as observed by Baldwin *et al.* (2003)) and in the models. One does not find this connection between variance and persistence of the AM in the troposphere alone. This suggests that the tropospheric AM becomes more persistent when there is stronger variability in the stratosphere; at these times, the longer time scales of the lower stratosphere can impact tropospheric persistence.

To confirm this connection between the lower stratosphere and troposphere, we repeat the analysis of Baldwin *et al.* (2003, *c.f.* Figure 2). **Figure 10.10** plots, as a function of height and season, the fraction of the variance of the next month's mean 850 hPa AM index, lagged by 10 days, that can be "predicted" from a persistence forecast based on today's instantaneous AM index. For example, the bullet of increased variance in the NH winter stratosphere suggests that information about the state of the NAM between 30 and 100 hPa is more useful for making forecast of next month's near surface NAM than knowledge of the near surface NAM itself. The consistency of the model biases toward a later seasonal cycle – in variance, time scales, and predictability – is particularly striking in the NH, and suggests that these phenomena are closely related. The predictability relationship in the SH is less clear. With the reanalysis, we have restricted analysis to the satellite era, which is a relatively short period leading to more uncertain correlations. With the models, the bias towards very long time scales leads to spurious predictability. Nonetheless, there is evidence of delayed and downward coupling between the lower stratosphere and the near surface, likely associated with the final warming of the vortex.

Gerber *et al.* (2008) found that the AM time scales in the CMIP3 models were relatively insensitive to climate trends. To assess the stability of the annular mode statistics in the CCMVal-2 models, we compared the late 20th century AM statistics (variance, time scales, and correlation structure) of the REF-B1 integrations with those based on the last five decades of the 21st century in the REF-B2 integrations (not shown). In general, we find that the statistics do not change much. The most significant exception is found in the variance structure of the SH stratosphere, where the period of peak variance shifts earlier in the season and weakens slightly. This is most likely due to the recovery of the ozone hole, which warms the spring/summer stratosphere, producing an earlier and more regular transition from westerlies to easterlies. In the NH, there is evidence that the peak AM time scales and the correlation structure shift earlier in the seasonal cycle, which could indicate increased variability in the winter and an earlier breakdown of the vortex. We note that the models have trouble getting the timing of the seasonal cycle correct in the observed period, so we must be cautious of over-interpreting these trends. In both hemispheres, however, these trends make the late 21st century simulations less biased compared to 20th century observations than the 20th century simulations themselves.

Up to this point we have focused on similarities in the model results. There is, however, significant spread between models. The AM *e*-folding time scales of each model at 100 and 500 hPa are shown in **Figure 10.11**. Individual models robustly capture the seasonal cycle of variability in both hemispheres, with the possible exception of the NH troposphere; the seasonal cycle of the tropospheric NAM, and evidence of downward coupling, are
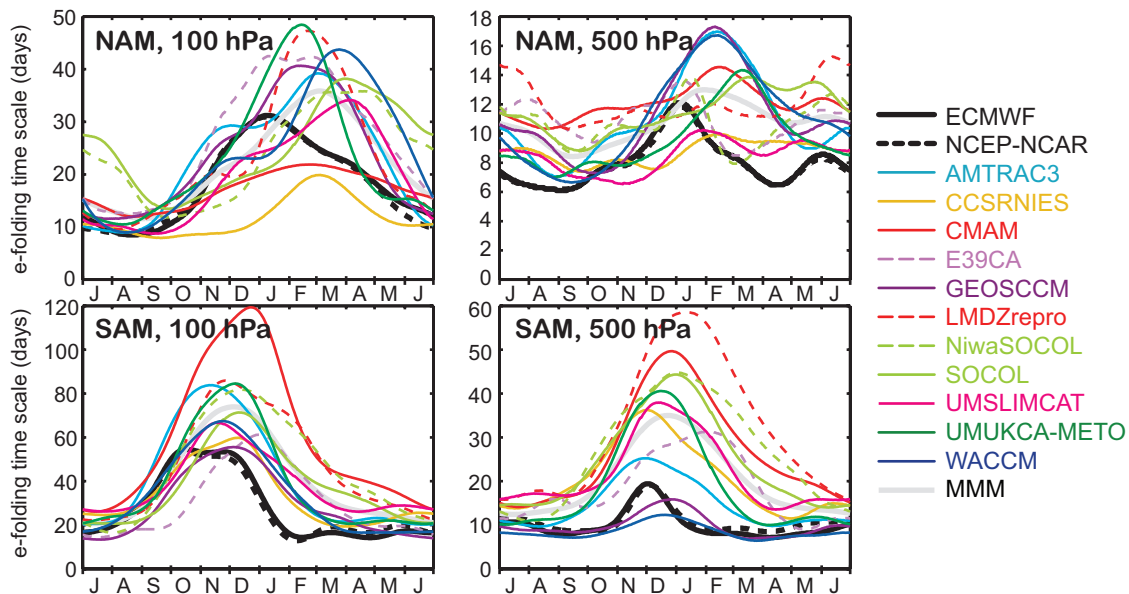

Figure 10.11: The annular mode *e*-folding time scale (left) in the lower stratosphere and (right) mid-troposphere as a function of season for the CCMVal-2 models: (top) NH, (bottom) SH.
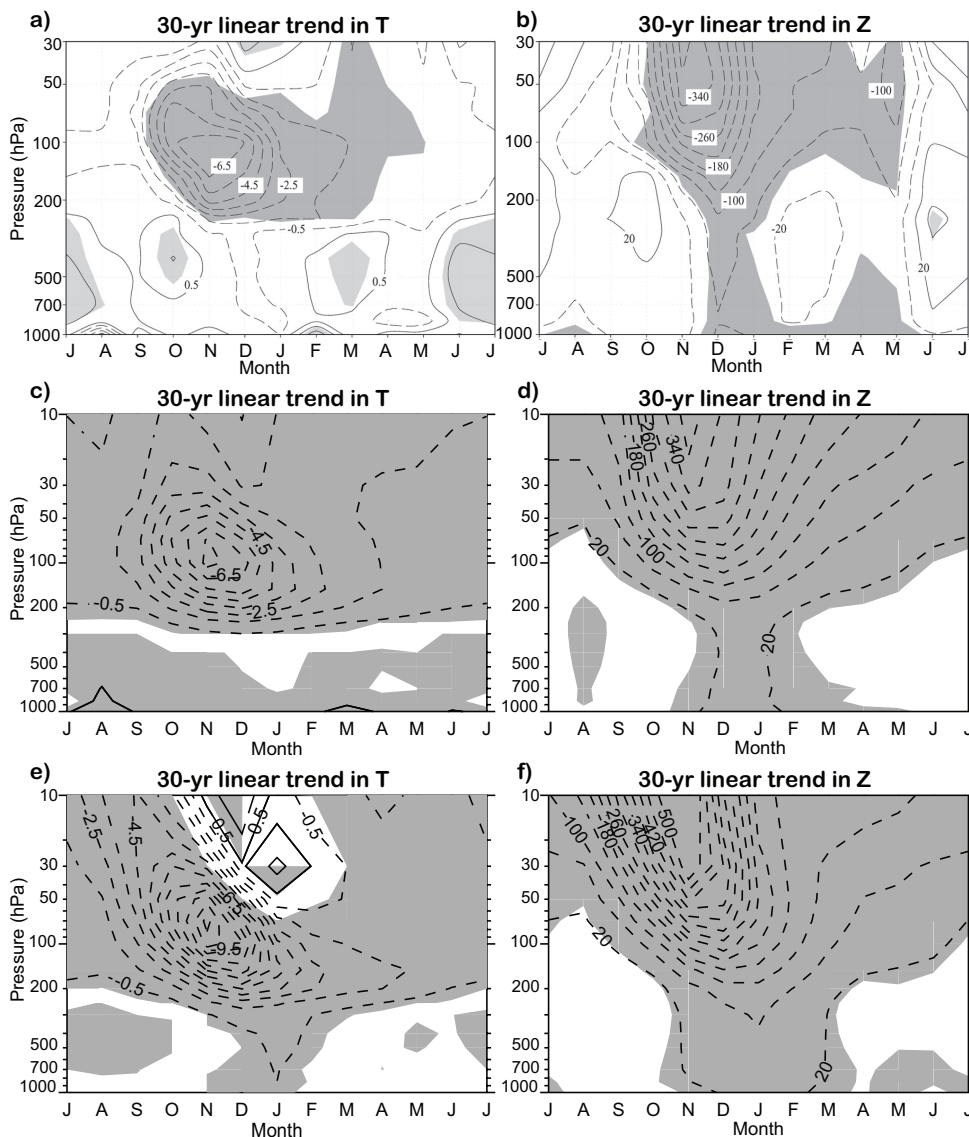
Figure 10.12: Seasonal cycle of linear trends (1969-1998) in (a,c,e) temperature (K per 30 years) and (b,d,f) geopotential height (m per 30 years) over the Antarctic. (a,b) observations (c,d) CMIP3 ozone ensemble average (e,f) CCMVal-2 (REF-B1) ensemble mean. Shading denotes trends that exceed one standard deviation of the respective monthly time series. The models used here are those listed in Figure 10.13 except HadCM3, whose simulations were driven by erroneously prescribed ozone forcing.

less clear in some models. It is also evident that the delay in the seasonal cycle and overestimation of time scales is a common bias. The SAM time scales vary by a factor of 2 in the stratosphere and a factor of 4 in the troposphere. It should be noted that GEOSCCM and WACCM, however, appear to match observations well. The vertical structure of their temporal variability (and that of many models) however differs slightly from observations. As seen in Figure 10.9, the SAM time scales in the reanalysis are relatively barotropic in the troposphere, while models tend to exhibit weaker persistence in the lower troposphere. We also note that their appears to be little correlation between model

biases in the NH and SH. For example, GEOSCCM and WACCM, noted above for their short SAM time scales, exhibit among the longest tropospheric NAM time scales.

The overestimation of time scales in the SH may influence the sensitivity of the models to external forcing, as suggested by the Fluctuation-Dissipation theorem (Gerber *et al.*, 2008). In particular, the tropospheric jets in models with long time scales may be more sensitive to external forcing. The biases and spread between the models suggest errors in model dynamics, especially in the SH, where coupling between the stratosphere and troposphere and/ or between eddies and the mean flow may be too strong.

Lastly, the unrealistic SAM time scales in the troposphere of many models may have implications for their representation of regional climate variability, particularly in the mid-latitudes.

10.4 Simulations of stratospheric influence on the troposphere in the past and future

10.4.1 Dynamical effects

10.4.1.1 Southern Hemisphere

The most often discussed and perhaps most important mode of influence of long-term stratospheric changes on the troposphere are the effects of changes in the stratospheric circulation on the tropospheric circulation, or dynamical effects. The last decades of the 20th century were marked by a significant change in the Antarctic tropospheric circumpolar circulation, with strengthening westerly winds and decreases in Antarctic geopotential height (Thompson and Solomon, 2002). The trends were largest in summer, lagging by 1-2 months similar trends in the stratosphere, which suggests a possible stratosphere-to-troposphere influence.

Figure 10.12 shows ensemble-averaged 1969-1998

temperature and geopotential height trends in the Antarctic in observations (Thompson and Solomon, 2002), in 13 CMIP3 models that include stratospheric ozone depletion, and in 17 CCMVal-2 models (REF-B1 simulations). Here and elsewhere in this chapter, trends shown are linear least squares trends. See **Figure 10.13** for the models and the number of realizations used. Consistent with the observations and CMIP3 simulations, the CCMVal-2 simulations show a maximum cooling at close to 100 hPa in November. However, the magnitude of the cooling is rather larger in the CCMVal-2 model mean, reaching 11 K, as opposed to ~7 K in the observations and the CMIP3 models. This discrepancy between models and observations is reduced by ~1 K if each model (rather than each simulation) is given equal weight, it is further reduced if the cooling is averaged over October-January at 100 hPa, and it is further reduced if the cooling is averaged over the whole of the Antarctic rather than at the locations of the radiosonde stations (see below). There is a large spread in this simulated cooling across the model ensemble, and no consistent bias in total ozone trend across the ensemble, but there is some indication that the CCMVal-2 models tend to simulate a larger stratospheric cooling for a given September-December total ozone trend compared to observations or the CMIP3 simulations (Figure 10.13). Note however, that the observed ozone trend used here is based on data from a single station (Halley), and therefore is relatively uncertain, and likely different to the Antarctic mean trend. EMAC, UMUKCA-METO, and UMUKCA-UCAM simulate too
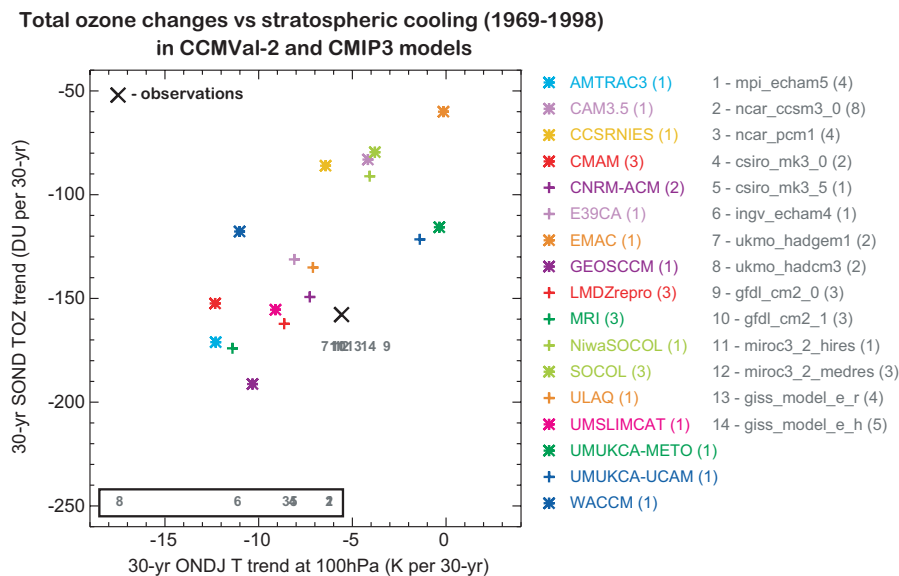

Total ozone changes vs stratospheric cooling (1969-1998) in CCMVal-2 and CMIP3 models

✳ AMTRAC3 (1)	1 - mpi_echam5 (4)
✳ CAM3.5 (1)	2 - ncar_ccsm3_0 (8)
✳ CCSRNIES (1)	3 - ncar_pcm1 (4)
✳ CMAM (3)	4 - csiro_mk3_0 (2)
+ CNRM-ACM (2)	5 - csiro_mk3_5 (1)
+ E39CA (1)	6 - ingv_echam4 (1)
✳ EMAC (1)	7 - ukmo_hadgem1 (2)
✳ GEOSCCM (1)	8 - ukmo_hadcm3 (2)
+ LMDZrepro (3)	9 - gfdl_cm2_0 (3)
+ MRI (3)	10 - gfdl_cm2_1 (3)
+ NiwaSOCOL (1)	11 - miroc3_2_hires (1)
✳ SOCOL (3)	12 - miroc3_2_medres (3)
+ ULAQ (1)	13 - giss_model_e_r (4)
✳ UMSLIMCAT (1)	14 - giss_model_e_h (5)
✳ UMUKCA-METO (1)	
+ UMUKCA-UCAM (1)	
✳ WACCM (1)	

Figure 10.13: 30-yr trends (1969-1998) in Antarctic September-December total ozone versus the October-January temperature trend at 100-hPa in 17 CCMVal-2 (REF-B1) models, 14 CMIP3 models including stratospheric ozone depletion, and observations. Observed temperature trends are based on Thompson and Solomon (2002) and ozone trends are based on measurements at Halley. CMIP3 ozone trends are shown for those models using Randel and Wu (1999) ozone. The temperature trends for CMIP3 models whose driving ozone trends were not reported or not available are shown in the black box in the lower part of the plot.

weak a stratospheric cooling and EMAC also simulates a total ozone trend that is too weak. The CCMVal-2 models also simulate a warming overlying the ozone-induced cooling, which is likely dynamical in nature (*e.g.*, Manzini *et al.*, 2003), and is just visible in the radiosonde observations, while being absent in the CMIP3 simulations, perhaps because of their limited stratospheric resolution.

The focus of this chapter is on coupling to the troposphere, and the second column of panels in Figure 10.12 shows that the simulated decrease in geopotential height is not limited to the stratosphere, but is also simulated in the troposphere, reaching a maximum in January in the CCMVal-2 models, two months after the maximum stratospheric cooling, and three months after the maximum stratospheric ozone depletion. Thus, consistent with earlier modelling studies (Gillett and Thompson, 2003; Arblaster and Meehl, 2006; Shindell and Schmidt, 2004; Karpechko *et al.*, 2008), the CCMVal-2 simulations simulate a clear downward propagation of the response to ozone depletion from the stratosphere to the troposphere. The tropospheric geopotential height response is somewhat weaker than that observed, but somewhat stronger than that simulated by the CMIP3 models. Concurrent with the tropospheric geopotential height response, and despite the prescribed SSTs in all but one model, the CCMVal-2 models simulate a tropospheric cooling over the Antarctic, consistent with the observed non-significant tropospheric cooling trend. The ensemble-mean cooling trend is larger than that simulated by the CMIP3 models, perhaps because of the larger cooling in the stratosphere.

Figure 10.14a shows ensemble mean zonal wind changes in the CCMVal-2 ensemble, and demonstrates that the historical simulated wind changes correspond to a poleward shift of the SH tropospheric jet in DJF. The ensemble mean simulated trends in the satellite era are remarkably similar to those estimated from reanalysis data, although the magnitude of the tropospheric trends is somewhat under-estimated (reanalysis data not shown).

Figure 10.16a shows that the simulated Antarctic cooling at 100 hPa in the CCMVal-2 models and CMIP3 models with ozone depletion agrees well with the observations, when averaged over October-January and with equal weight given to each model. Observations of October Antarctic column ozone depletion lie within the spread of CCMVal simulations (Chapter 9). A close correlation is seen between SOND ozone depletion and the ONDJ 100-hPa Antarctic temperature trend (**Figure 10.15a**), and a similarly high correlation is seen with the DJF tropopause pressure trend (Figure 10.15b). Cooling in the lower stratosphere increases the temperature lapse rate near the tropopause, pushing the height of 2 K/km temperature lapse rate upward (this lapse rate is used to define the tropopause here) (Santer *et al.*, 2003; Son *et al.*, 2009a).

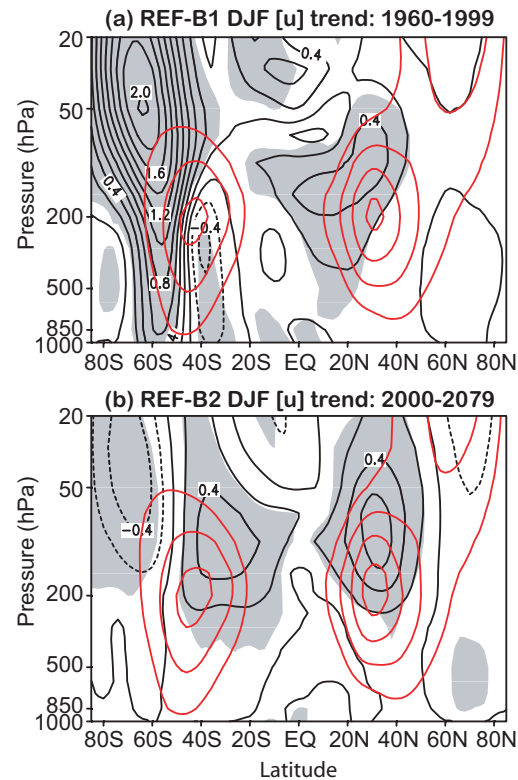Figure 10.15c shows the latitudinal shift of the wind

Figure 10.14: Long-term mean (orange) and linear trend (black contour) of the DJF-mean zonal-mean zonal wind (a) for the time period of 1960-1999 in REF-B1 runs, and (b) for the time period of 2000-2079 in REF-B2 runs. Contour intervals are 10 m/s starting from 10 m/s for the climatology and 0.2 m/s/decade for the trend. Zero lines are omitted and values greater than one standard deviation are shaded.

maximum in DJF at 850 hPa in each of the CCMVal-2 models and demonstrates that this is correlated with the SOND ozone depletion simulated in the same model, indicating that the amount of stratospheric ozone depletion is the dominant factor controlling the size of the tropospheric circulation change in each model. Past trends in the DJF tropospheric circulation have clearly been forced in part by ozone, though part of the trend has also been attributed to increasing greenhouse gases (Marshall *et al.*, 2004; Arblaster and Meehl, 2006). While increasing greenhouse gases in the future are expected to lead to a further poleward intensification of SH tropospheric winds in DJF, future ozone recovery is expected to act in the opposite sense (*e.g.*, Son *et al.*, 2008). Figure 10.15a demonstrates that at 100 hPa in the future, stratospheric ozone recovery exerts the dominant influence on stratospheric temperature, with a simulated warming which is approximately proportional to the amount of ozone recovery simulated in the first half of the 21st century (Son *et al.*, 2008). However in the troposphere the effect of ozone recovery on the circulation is likely to be largely cancelled out by the effect of green-

house gas increases in DJF, and no significant shift in the jet location at 850 hPa is seen (Figure 10.14b and 10.15c). Figure 10.16b contrasts the shift in the tropospheric jet in the 21st century simulated in the CCMVal-2 models with that simulated in the CMIP3 models with and without changes in stratospheric ozone. Those CMIP3 models with no future ozone changes, but continued greenhouse gas increases simulate a southward shift in the DJF jet location, in contrast to little change in the jet location in those CMIP3 models with specified ozone recovery and in the CCMVal-2 simulations. Note that, in contrast to CCMVal-1 (Son *et al.*, 2008), there is only a small and non-significant northward shift in DJF jet location in the 21st century in the CCMVal-2 ensemble mean. The reason for this difference in behaviour between the CCMVal-1 and CCMVal-2 simulations remains to be determined. The jet location trends simulated in the 21st century in the CCMVal-2 models are consistent with those simulated in the CMIP3 models with stratospheric ozone recovery (Figure 10.16).

Figure 10.16c demonstrates that both CCMVal-2 models and CMIP3 models simulate a poleward expansion of the SH Hadley cell in the last decades of the 20th century (Lu *et al.*, 2007; Seidel *et al.*, 2008). Changes in the width of the Hadley Cell are of particular interest because of their potential impacts on precipitation patterns (Seidel *et al.*, 2008). Previous research has mainly focused on the role of greenhouse gases in forcing this trend, but the results presented here both for the CMIP3 models with and without ozone depletion (Figure 10.16c), and for the CCMVal-2 simulations (Figure 10.15d and Figure 10.16c), demonstrate an important role for stratospheric ozone depletion in driving the broadening of the Hadley Cell in DJF (see also Son *et al.*, 2009b). Observed broadening of the Hadley Cell is larger than that simulated by the CMIP3 models (Seidel *et al.*, 2008): These results suggest that stratospheric ozone depletion, not included in many of the CMIP3 models, may help to explain this discrepancy. In JJA, when stratospheric ozone depletion is small, the CCMVal-2 simulations and the CMIP3 simulations all exhibit similar broadening trends (Figure 10.16f). Future greenhouse gas increases
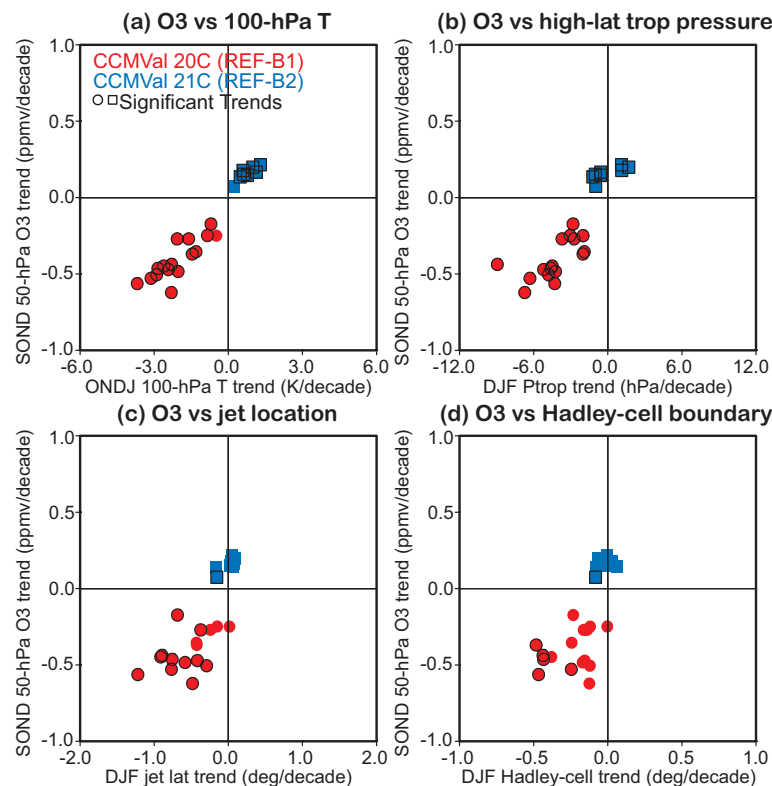

Figure 10.15: Trend relationship between SOND-mean ozone at 50 hPa integrated south of 64°S and variables of interest: (a) ONDJ-mean temperature at 100 hPa integrated south of 64°S, (b) DJF-mean extra-tropical tropopause pressure integrated south of 50°S, (c) location of the DJF-mean zonal wind maximum at 850 hPa, and (d) location of the SH Hadley cell boundary at 500 hPa. Linear trends are computed for the time period of 1960-1999 in the REF-B1 runs (red circles) and for the time period of 2000-2079 in the REF-B2 runs (blue squares). Trends which are statistically significant at the 95% confidence level are bounded in black. Significance is tested with the method used in Santer et al. (2000). Note that the 20th century trends are calculated over a 40-yr period compared to an 80-yr period for the 21st century trends, likely explaining their larger variability.
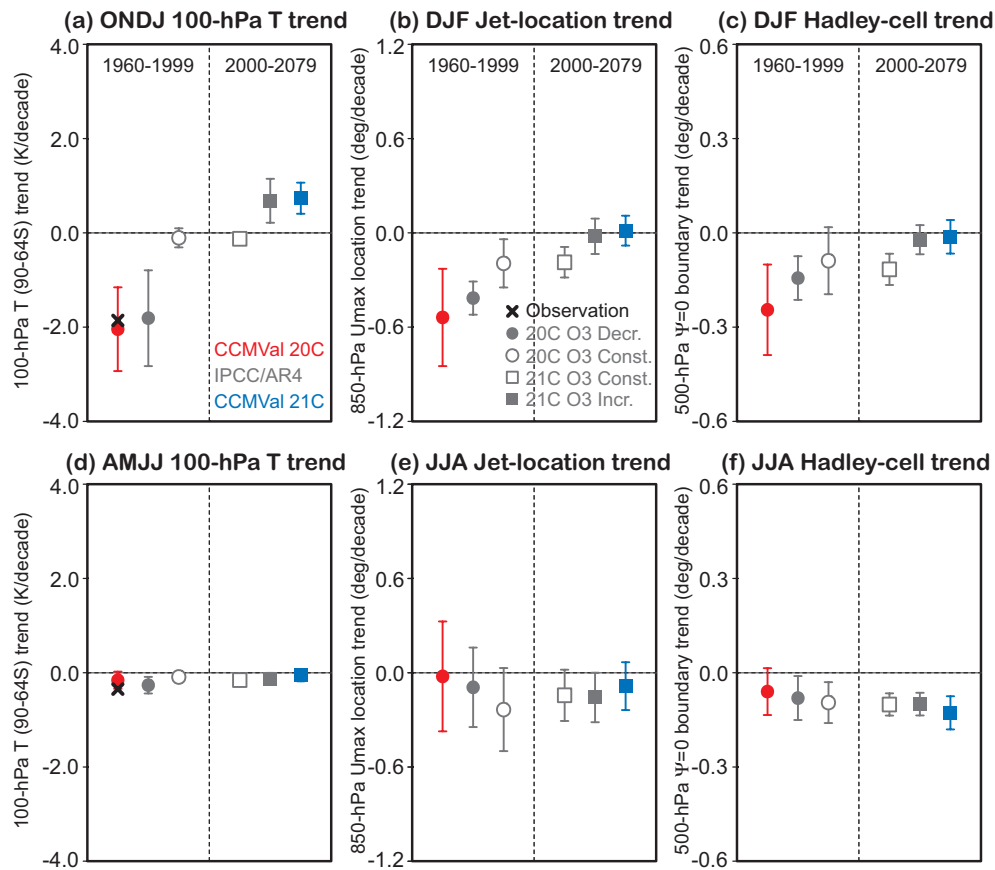
Figure 10.16: SH circulation changes as simulated by the CCMVal-2 models and CMIP3 models. The multi-model mean trends are shown with one standard deviation for (a) ONDJ-mean temperature at 100 hPa integrated south of 64°S, (b) location of the DJF-mean zonal-mean zonal wind maximum at 850 hPa, (c) location of the DJF-mean SH Hadley-cell boundary at 500 hPa, (d-f) same as (a-c) but for AMJJ, JJA, and JJA, respectively. In (a,d), observed temperature trends between 1969 and 1998 (Thompson and Solomon, 2002) are shown in crosses. The negative values in (b-c, e-f) denote a poleward shift of the westerly jet or a poleward expansion of the Hadley cell. Uncertainty bars show one standard deviation for each set of models.

are expected to drive a continuing poleward expansion of the Hadley Cell (Seidel *et al*., 2008), but the results presented here indicate that this effect may be offset by the effects of stratospheric ozone recovery in DJF in the SH, with the CCMVal-2 models simulating little change in the width of the SH Hadley Cell in this season (Figure 10.15d and Figure 10.16c).

10.4.1.2 Northern Hemisphere

Figure 10.14a shows few regions of significant trends in NH extratropical DJF zonal-mean-zonal wind in the CCMVal-2 model mean for the 1979-1999 period. In the 2000-2079 period (Figure 10.14b) a strengthening of the subtropical jet is seen in the upper troposphere and lower stratosphere, but with few regions of significant zonal wind change in the lower troposphere. Arctic average geopoten-

tial and temperature trends in the CCMVal-2 simulations of the past do not show a clear downward propagating trend signal of the type shown in the SH in Figure 10.12 (not shown). However, a regression analysis of the NAM index onto hemispheric mean total column ozone and CO_2 indicated significant co-variability between ozone variations and the near-surface NAM index in winter and spring, and also significant covariability between Cl_y at 50 hPa and the near-surface NAM, taking the ensemble of models together (Morgenstern *et al*., 2010). Results are therefore suggestive of a role for ozone depletion in forcing long-term changes in the NAM in the CCMVal-2 models.

10.4.2 Radiative effects

Stratospheric changes in temperature and composition influence the troposphere and surface not only through

dynamical mechanisms, but also more directly through changes in the radiative fluxes between the stratosphere and troposphere. Stratospheric ozone depletion has contributed to an increase in surface UV radiation (WMO/UNEP, 2007), it is a contributor to global radiative forcing (*e.g.*, Forster *et al*., 2007), and the radiative influence of ozone depletion on the troposphere has been proposed as a mechanism to explain tropospheric cooling over Antarctica (Grise *et al*., 2008; Keeley *et al*., 2007). Some of these effects are investigated in the CCMVal-2 models here.

10.4.2.1 The response of surface UV radiation to stratospheric ozone changes

Total column ozone and vertical profiles of ozone and temperature from the REF-B1 and REF-B2 runs of the CCMVal-2 models were used to calculate solar ultraviolet radiation levels at the surface in the second half of the

20th and through the 21st century using the UVSPEC model (Mayer and Kylling, 2005; Tourpali *et al*., 2009). While column ozone is the dominant driver of erythemal UV variations, ozone profile, and to a lesser extent temperature changes, also contribute to the changes in erythemal UV, especially in the polar regions. Surface UV reflectivity was set to a climatological mean, calculated from the Total Ozone Mapping Spectrometer (TOMS) surface UV reflectivity (Herman *et al*., 1997). For the tropospheric aerosol optical depth, we used the AeroCom climatology (Kinne *et al*., 2006), and a fixed cloud distribution was assumed. All results are presented here as departures (in %) from the corresponding monthly means of the 15-year average of the period 1965 through 1979.

Figure 10.17 shows changes in UV radiation calculated from the REF-B1 runs, representing past changes in ozone. Starting in the early 1980s, surface erythemal irradiance is found to increase globally (earlier at high southern latitudes), as a result of the ozone decline. These results
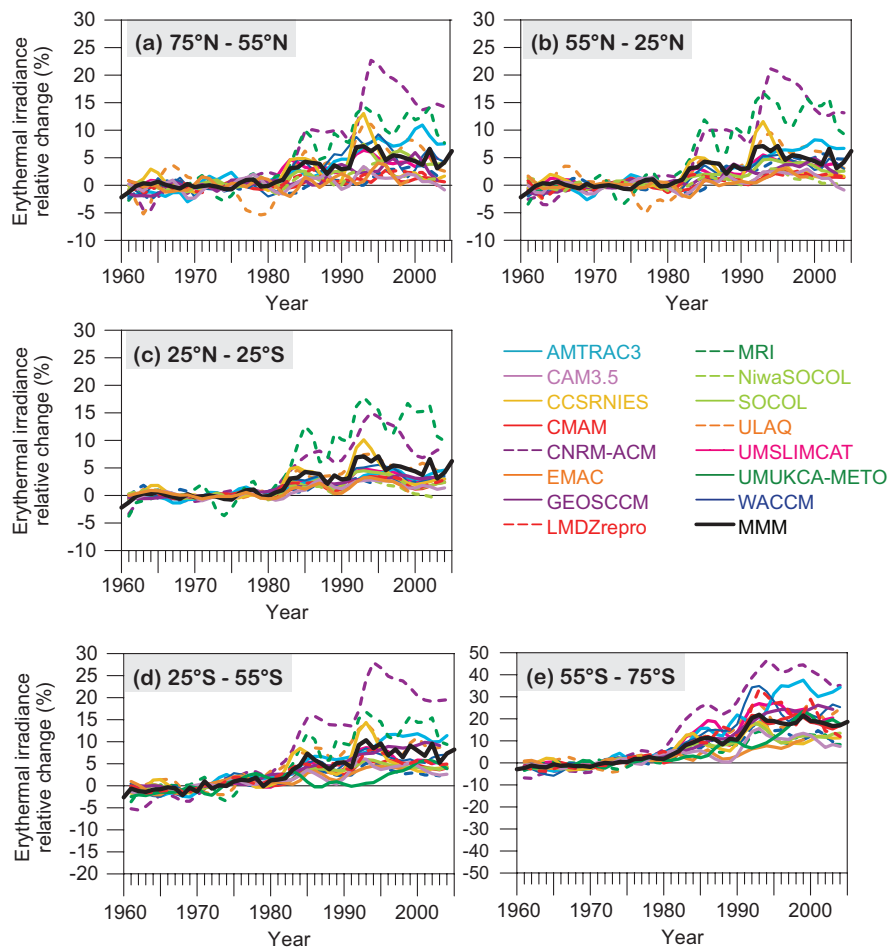

Figure 10.17: REF-B1 Runs: Annual means of surface clear-sky erythemal irradiance changes (in %, relative to 1965-1979) for five latitude belts: (a)75°N-55°N, (b)55°N-25°N, (c)25°N-25°S, (d)25°S-55°S and (e) 55°S-75°S. The model names are indicated in the centre panel. The black line represents the multi-model average.

Figure 10.18: REF-B2 runs. Annual means of surface clear-sky erythemal irradiance changes (in %, relative to 1965-1979) for five latitude belts: (a)75°N-55°N, (b)55°N-25°N, (c)25°N-25°S, (d)25°S-55°S and (e) 55°S-75°S. The model names are indicated in the centre panel. The black line represents the multi-model average.
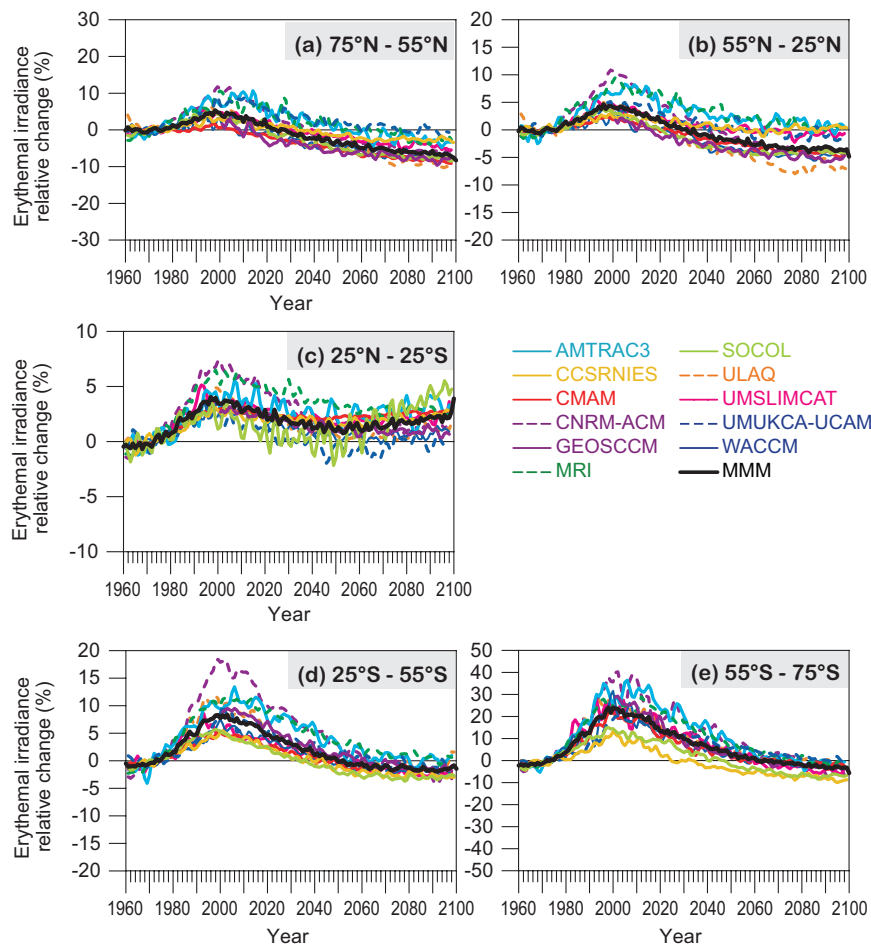
are related to variations in column ozone shown in Chapter 9: For example, MRI and CNRM-ACM have larger than average tropical ozone losses (Section 9.3.4), and hence a larger increase in tropical UV. The ozone-induced effect of the El Chichón and Pinatubo eruptions on surface UV radiation is clearly seen at all latitudes, including the tropical regions.

Figure 10.18 presents the changes in UV radiation calculated from the REF-B2 runs, representing projected future changes in ozone. Starting around 2005, the surface erythemal irradiance is projected to decrease globally as a result of ozone recovery. The magnitude of these decreases varies with latitude and is more pronounced in areas where the most ozone depletion currently occurs, such as the Antarctic. In the tropics, erythemal UV is projected to increase towards the end of the 21st century, a trend related to a decrease in column ozone associated with an acceleration of the Brewer-Dobson circulation (Hegglin and Shepherd, 2009).

Figure 10.19 presents the evolution of the zonal-mean erythemal irradiance in the polar regions (75° - 90°) of both hemispheres. The top panel (a) presents the changes in surface erythemal irradiance in the southern polar latitudes and for the months October – November, the time when the Antarctic ozone hole reaches its maximum in area and intensity. All models show large interannual variability in this latitude belt and months, larger than at all other latitude belts, with surface erythemal irradiance reaching pre-1980 levels only after 2070. The bottom panel (b) presents the evolution of surface erythemal irradiance in the northern polar region during late winter-early spring (March-April). The interannual variability is large as well, but smaller than in the SH. The magnitude of the changes is much smaller than in the south (note the different scales used), and pre-1980 levels are reached earlier (~ 2050): this is consistent with the earlier return to pre-1980 ozone levels in the Arctic (Figure 9.20). The changes described here reflect the corresponding changes in the simulated ozone fields
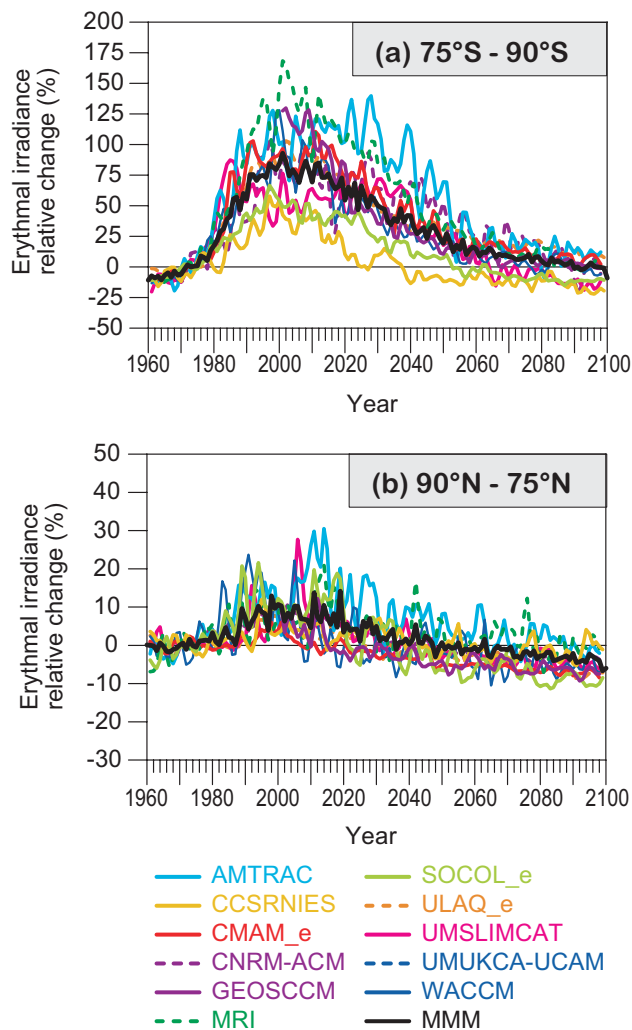
Figure 10.19: (a) Average of surface erythemal irradiance for October - November at 75°S-90°S. (b) same as in (a) but for March - April at 90°N-75°N.

(Section 9.5.3), and are strongly influenced by changes in stratospheric circulation (Hegglin and Shepherd, 2009).

As climate change is likely to affect future cloudiness, the change in cloud transmittance (or cloud modification factor) was calculated as the change in the ratio of surface shortwave flux under all skies over the flux under clear skies. Here data provided by 8 runs of 5 CCMs were used. The cloud transmittance derived from the models was compared to results from a similar analysis performed using data from 11 CMIP3 models, and good agreement was found over the 2001-2100 period. The shortwave cloud transmittance was converted to erythemal UV cloud transmittance, and our analysis was extended to the calculation of changes in surface erythemal solar irradiance under all-sky conditions.

Figure 10.20, top panels, presents the changes in surface erythemal solar irradiance for the months of January

(left panels) and July (right panels) under clear-sky conditions. The 20-year period 2080-2099 is shown, relative to the base-period of 1965-1979, before total ozone started its continuous decline. The bottom panels present the changes for the same months, but for all–sky conditions (*i.e.*, taking into account changes in cloudiness in the troposphere). While ozone is mainly responsible for the latitudinal changes of erythemal irradiance, cloud effects result in a more complex pattern with alternating regional positive and negative changes during the 21st century.

Generally, as is also seen in the clear-sky conditions case (top panels), erythemal irradiance is projected to increase in the tropics, and to decrease in the mid- and high latitudes of both hemispheres. The positive response in the tropics becomes larger when the effect of clouds is taken into account. Large reductions in surface irradiance (-10 to -15%) are calculated for the second half of the 21st century in specific regions of the high northern latitudes, as well as over Antarctica. Large increases in erythemal irradiance (10-15%) appear in tropical regions of south-east Asia and Central America, with more moderate increases over southern Europe in summer.

During the late 20th century (not shown) the effects of ozone depletion on erythemal solar irradiance are apparent with a more uniform pattern of small to moderate increases in irradiance across the globe. Particularly in Antarctica, the strong ozone depletion dominates surface erythemal irradiance changes over the cloud effects leading to strong increases of up to 15%.

10.4.2.2 Radiative forcing due to stratospheric ozone changes

CCMs predict concentrations of chemically active species and model their radiative effects on atmospheric temperatures, yet they do not allow the effects of changes in individual species on tropopause radiative forcing to be evaluated directly. Stratospheric ozone changes since the 1970s are believed to have led to a small negative radiative forcing of around -0.05 Wm^{-2} with a 0.1 Wm^{-2} uncertainty range (Forster *et al.*, 2007). Stratospheric water vapour and methane changes can also be a significant source of forcing. The Forster *et al.* (2007) estimate is based on relatively few radiative calculations and ozone data sets.

Here we use an offline version of a single radiation code (Edwards and Slingo, 1996) to evaluate the radiative forcing from ozone changes predicted by the models' REF-B1 integration using their monthly averaged ozone fields. We assume clear skies and evaluate the radiative forcing using the Seasonally Evolving Fixed Dynamical Heating (SEFDH) approximation (Forster *et al.*, 1997). We fix the dynamical heating at the models' 1960 values and time-step the stratospheric temperatures forward using daily time steps, updating the ozone or other trace gas values
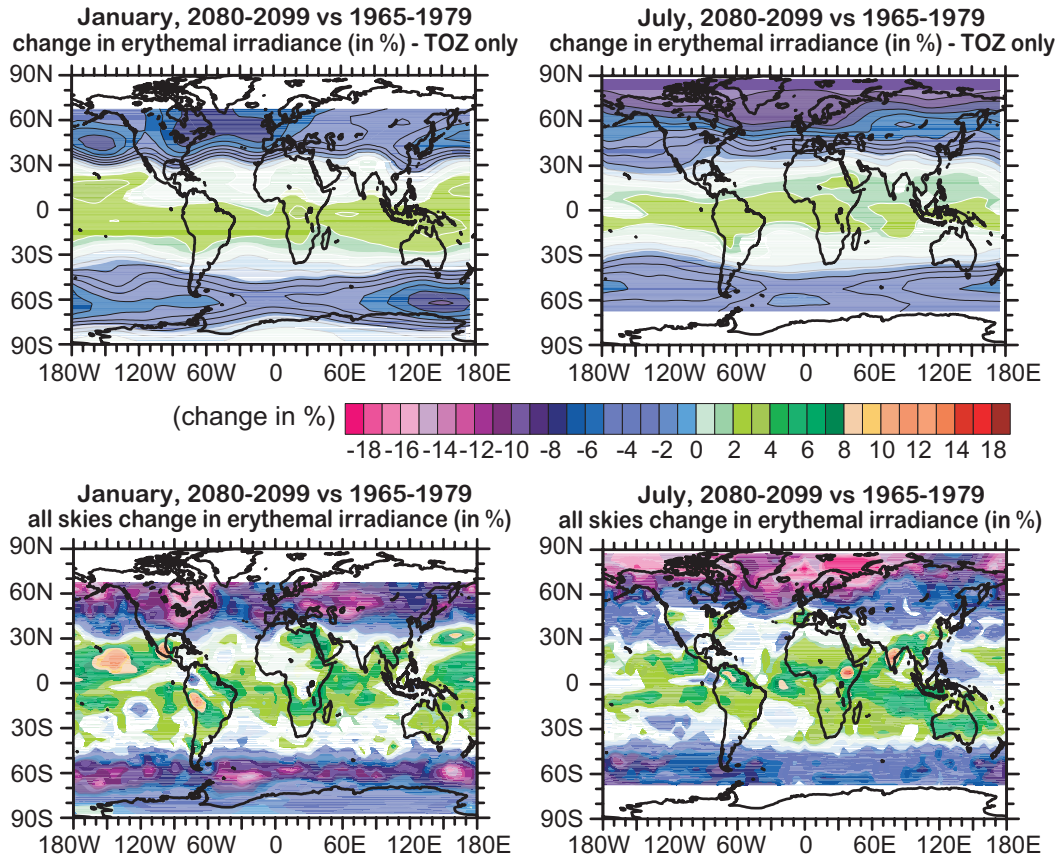
Figure 10.20: REF-B2 Runs. 20-year averages of clear-sky (top) and all-sky (bottom) erythemal irradiance changes (%) for January (left panels) and July (right panels) with respect to the 1965-1979 average. Calculations refer to local noon values and changes reflect the predicted changes in total ozone (11 CCMs provided 18 runs in total) and cloud transmittance (8 runs by 5 CCMs). In the top panels, small but positive changes appear in the tropics, and are statistically significant (95% level) over the equator. In the bottom panels, coloured areas denote statistically significant changes. Areas with insignificant changes are left blank.

each day by interpolating between monthly average values.

Figure 10.21 shows global mean shortwave, long-wave and total radiative forcing anomalies relative to 1960-1969 due to ozone changes based on 16 CCMVal-2 REF-B1 simulations. Over this period there is a clear upward trend in SW forcing, associated with decreased absorption of UV in the stratosphere, and a downward trend in LW forcing, associated primarily with stratospheric cooling (Grise *et al.*, 2009). The ensemble mean trend in total radiative forcing due to ozone is small but positive, and individual simulations show a large range of trends, including some simulations that show positive trends. This spread is much larger than the uncertainty range on the radiative forcing trend due to observed ozone changes given by Forster *et al.* (2007). It remains to be determined whether this is because some models have unrealistic ozone changes, or whether this is because Forster *et al.* (2007) under-estimated the uncertainty in ozone-induced radiative forcing. The radiative forcing of volcanically-induced ozone changes is also apparent, particularly the decrease in total ozone-induced

radiative forcing following the eruption of Mt Pinatubo in 1991 (the radiative effects of the aerosols themselves are not accounted for here).

10.4.3 Chemical effects

Lastly, the stratosphere may influence the composition of the troposphere through changes in the fluxes of chemical constituents across the tropopause. The most important such flux is the ozone flux associated with stratosphere-troposphere exchange (STE).

10.4.3.1 Stratosphere-to-troposphere ozone fluxes

While the contribution of stratospheric ozone to the total tropospheric ozone budget is only about 10%, it strongly affects ozone concentrations in the upper troposphere (Stevenson *et al.*, 2006; Denman *et al.*, 2007), where ozone has a relatively long lifetime of about one
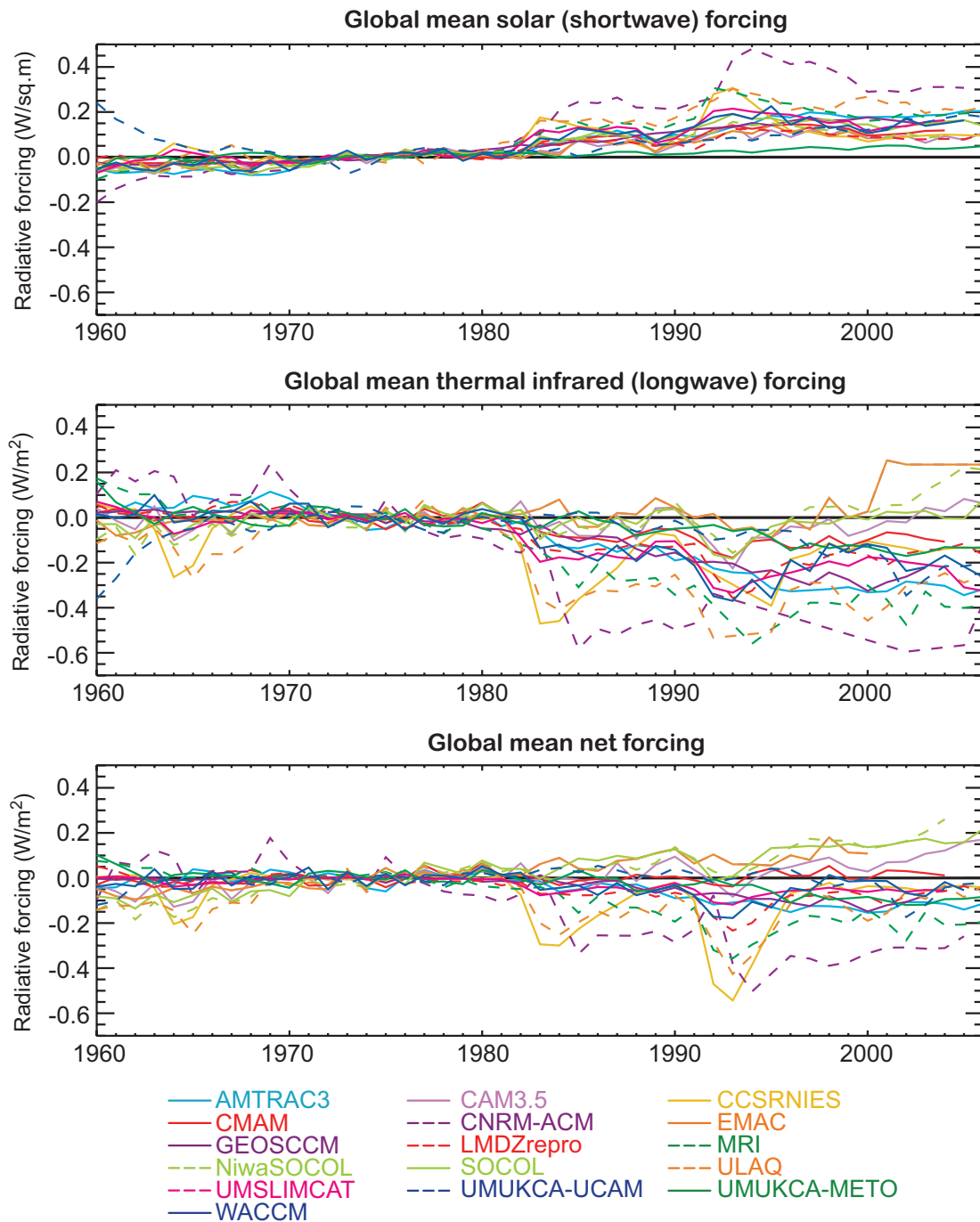
Figure 10.21: Calculated changes in global mean ozone-induced radiative forcing evaluated at the tropopause based on simulated ozone in 16 REF-B1 simulations and a fixed dynamical heating model. (a) SW forcing, (b) LW forcing, and (c) total forcing. Anomalies with respect to the period 1970-1979 are shown.

month and also the greatest impact on the radiative forcing of surface temperatures (Forster and Shine, 1997).

CCMs consistently predict an increase in the strength of the Brewer-Dobson circulation due to climate change (Butchart *et al.*, 2006; McLandress and Shepherd, 2009; see also Chapter 4). It has also been shown that this in-

crease strongly affects the distribution of stratospheric ozone, especially in the mid-latitude lower stratosphere (Shepherd 2008; Li *et al.*, 2009). These changes in the ozone distribution will affect the amount of ozone transported from the stratosphere into the troposphere, which is why it is important to use stratosphere-resolving, fully

interactive CCMs to quantify the impact of climate change on STE ozone fluxes, and to separate its effect from that of ozone depletion and recovery (Hegglin and Shepherd, 2009). Note that most of the tropospheric CCMs used for the IPCC AR4 to examine future changes in STE ozone fluxes had poor vertical resolution within the stratosphere and generally relaxed stratospheric ozone to prescribed values (Denman *et al.*, 2007).

STE ozone fluxes are generally calculated in one of two ways. The first and most direct method is to calculate the STE ozone flux across the tropopause using instantaneous model fields with high temporal resolution. However, these calculations have been shown to be very sensitive to the particular tropopause definition used (Stevenson *et al.*, 2004). This is presumably because the net ozone flux is a small difference of large terms, as a result of the small-scale two-way (*i.e.*, reversible) transport into and out of the lowermost stratosphere. It is moreover an impractical calculation for a multi-model comparison with restricted data availability such as CCMVal-2. The second method is to infer the STE ozone flux as a residual in the tropospheric ozone budget. That calculation, too, involves a small difference of large terms, and it is also not possible with the fields saved in CCMVal-2. However, Holton *et al.* (1995) argued that the stratosphere-to-troposphere flux of any long-lived tracer (including ozone) is controlled by the Brewer-Dobson circulation, since any material that descends across a particular control surface (*e.g.*, 100 hPa) must, in the absence of sources and sinks within the lowermost stratosphere, eventually make it into the troposphere.

The STE ozone fluxes (F_{STE}) are therefore calculated for each hemisphere on a monthly mean basis using a simple box-model approach previously used for mass flux calculations (Appenzeller *et al.*, 1996), but applied instead to ozone (Hegglin and Shepherd, 2009):

$$F_{STE} = F_{100hPa} - dM_{LMS}/dt \qquad (10.4)$$

Here F_{100hPa} is the downward flux of ozone across the 100-hPa surface, estimated as the area-weighted integral within each hemisphere of the zonal-mean ozone concentration multiplied by the residual vertical velocity $\overline{w}^*$, and M_{LMS} is the total mass of ozone contained in the lowermost stratosphere (defined as the region between the 100-hPa surface and the thermal tropopause). The STE ozone flux, F_{STE}, is then calculated as a residual. The advantage of this method (as with the Appenzeller *et al.* (1996) method for mass flux) is that the terms contributing substantially to F_{100hPa} are mainly of the same sign. In this calculation, chemical processes between the tropopause and 100 hPa are assumed to have a negligible impact on F_{STE}. This is a reasonable assumption for global fluxes because the photochemical lifetime of ozone is generally much longer than its residence time in this region (Olsen *et al.*, 2004). The largest error would come from the effect of the ozone hole,

which would lead to an overestimation of the STE ozone fluxes, but only during the period of ozone depletion/recovery. In any case, so long as the calculation is done the same way for all models and for observations, it serves as a consistent and readily calculated diagnostic.

Figure 10.22 shows the long-term evolution of the STE ozone fluxes for all the CCMVal-2 models which provided the necessary data. In total, data from nine REF-B2 model simulations were available. For CMAM, CCMVal-1 results were used instead of CCMVal-2, as they are believed to be more realistic[1]. An observational estimate from 1991-2002 is also provided (black dots) using the ERA-Interim reanalysis together with the monthly resolved ozone climatology of McPeters *et al.* (2007).

Figure 10.22a shows that the calculated global STE ozone fluxes during the 1990s for the different models are generally somewhat larger, by up to 30%, than those based on the observations. The latter are seen to be in the middle of the (rather uncertain) observational range given by Denman *et al.* (2007), shown by the black vertical bar, which was obtained using different calculation methods. This provides confidence in our diagnostic method. Note that apart from ULAQ, which is well below the observational range, the STE ozone fluxes in the CCMVal models tend to lie in the upper half of the range provided by the tropospheric models (Stevenson *et al.*, 2006). The consistently larger ozone fluxes obtained in most of the models may stem from a high bias of around 10-20% in ozone at 100 hPa as can be seen in Chapter 7, Figures 7.22 and 7.23.

SOCOL, MRI, and CCSRNIES are, aside from ULAQ, the models with the largest differences in the global fluxes when compared to the observations (using this method). The best agreement is found for GEOSCCM, with only a small under-estimation of the STE ozone fluxes in the SH when compared to the observations, also reflected in the global mean. Note that in order to cover the period between 1960 and 2100, the REF-B2 run of GEOSCCM did have to be extended into the past using the REF-B1 run. These two runs do not merge exactly into each other, which will have a slight impact on the trend estimation between the future and the past.

In both the NH and the SH, the model fluxes are generally larger than the observations as reflected in the global flux. The spread between the different models is higher in the NH than in the SH. In the NH, the largest differences are seen between the observations and SOCOL, MRI, and CCSRNIES. In the SH, these models are close to the rest of the models during the past, but exhibit anomalously strong fluxes towards the end of the current century. The NH flux

[1] *For CCMVal-2, CMAM was coupled to an ocean model. Changes to the model made to enforce energy balance for coupling led to a degradation of the stratospheric dynamics, for reasons that are not fully understood (see also Chapter 4).*
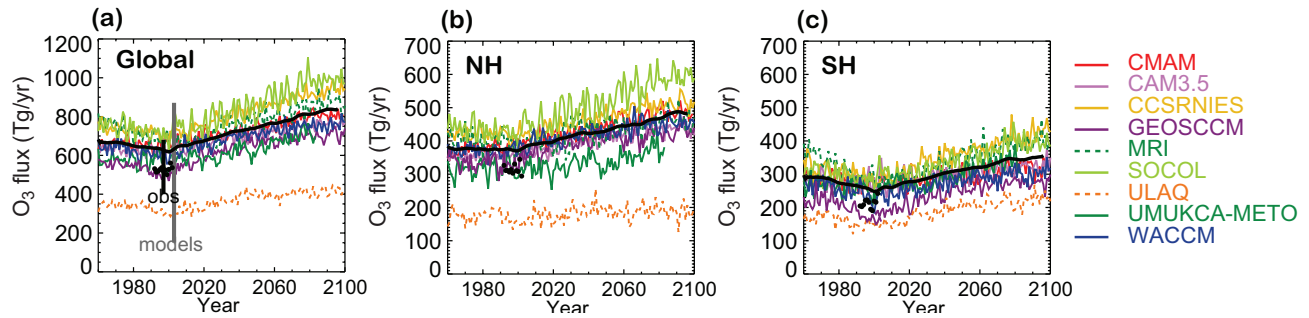
Figure 10.22: Multi-model comparison of the time evolution of (a) global, (b) northern hemispheric, (c) southern hemispheric stratospheric ozone flux into the troposphere between 1960 and 2100 derived from CCMVal-2 models. Coloured lines denote different models as given in the colour code, and the black line denotes the multi-model mean. The black uncertainty bar indicates the observational range given in the IPCC AR4 report (Denman et al., 2007), the grey uncertainty bar the tropospheric model range given in Stevenson et al. (2006). Black dots indicate observations calculated from ERA-Interim data together with the ozone climatology of Mc-Peters et al. (2007) using the same method as used for the CCMs.

is about 30% larger than the SH flux in both observations and models, except for ULAQ. The multi-model mean (thick solid black line) is calculated excluding ULAQ, since this model obtained the lowest scores in the metrics of Chapter 7 relevant for a good performance in simulating STE ozone fluxes. The multi-model mean is biased high in both hemispheres and also in the global mean, relecting the single model behaviour.

Simulated past and future STE ozone flux changes are influenced both by changes in stratospheric dynamics due to climate change and by ozone depletion and recovery, though to different degrees in the different models and in the two hemispheres. The changes over three time periods are given in **Table 10.3**. The multi-model mean of the change in the STE ozone flux attributable to climate change (1965-2095) is slightly larger in the NH (26%) than in the SH (21%). The multi-model mean change in global STE ozone flux between 1965 and 2095 is consistent in terms of percentage changes with the CMAM result shown in Hegglin and Shepherd (2009), however, its changes calculated for the NH and SH are smaller and larger, respectively. Over the period 2000-2030, the CCMVal-2 models show increases in the global ozone flux of 73.3 (±3.6) Tg/year or 11.7 (±0.6) %, which is towards the upper end of the range from tropospheric models of 41 (± 31) Tg/year or 7.6 (± 5.7) % reported by Stevenson *et al*. (2006). The results are expected to be dependent on the choice of the models that are included in the calculation of the mean.

10.5 Summary

10.5.1 Summary by Model

Multi-model mean: On average, the CCMVal-2 models simulated the mean climate and variability of the zonal mean *u*, *v*, and *T* fields well. CCMVal-2 models were only slightly better than CCMVal-1 models overall. However, the stratospheric simulations using CCMVal-2 models were much better thanthose of the CMIP3 models. There was no clear improvement in the simulation of the mean or variability in the extra-tropics in models which included a simulated or nudged QBO. The performance skill (based on *u*, *v*, and *T*) was better in the NH than the SH, with a fairly large spread among models.

The NAM and the SAM were very well simulated by nearly all the CCMVal-2 models, especially in the troposphere. Both the latitudinal pattern and the amplitude of the patterns tended to be similar to the observations. In the stratosphere, the multi-model mean annular modes, as well as their variability, were close to the observations. However, there was a large inter-model spread. The CMIP3 models were inferior to all the CCMVal-2 models in the stratosphere.

Downward propagation of NAM and SAM signals was observed in all models, with the average tropospheric effect being slightly stronger than in the observations. However, there is uncertainty in the observations due to the short observational record.

On average, the CCMVal-2 simulation of the seasonal cycle of the variance of the NAM and SAM was realistic, except that the models tend to have a cold-season maximum that is delayed by roughly one month. There is large variability in how well the CCMVal models simulate the persistence (*e*-folding time scale) of the NAM and SAM. The models tend to have time scales that are too long, in both the troposphere and lower stratosphere. Some models had SH time scales up to four times that observed.

In the SH, the 1969-1998 trends in *Z* (geopotential height) and *T* capture the observed cooling that extends to the surface. Although the average modelled ozone trend was less than that observed at 100 hPa, the *T* trend at 100

Table 10.3: Multi-model mean of absolute and relative changes in global, northern, and southern hemispheric ozone fluxes for different time periods (corresponding to ozone depletion (1965-2000), ozone recovery (2000-2035), and climate change (1965-2095)). For the calculation of the mean, the ULAQ has been excluded. For models providing more than one simulation, the ensemble means have been used.

	Time period (yr)	O$_3$-flux change (Tg yr-1)	O$_3$-flux change (%)
Global	1965-2000	-40.8 (±2.7)	-6.1 (±0.4)
	2000-2035	73.3 (±3.6)	11.7 (±0.6)
	1965-2095	169.0 (±5.4)	24.1 (±0.8)
NH (0°N-90°N)	1965-2000	-2.8 (±1.6)	-0.7 (±0.4)
	2000-2035	39.8 (±1.9)	10.6 (±0.5)
	1965-2095	108.4 (±3.8)	26.2 (±1.0)
SH (0°S-90°S)	1965-2000	-38.0 (±1.6)	-13.0 (±0.5)
	2000-2035	33.5 (±1.9)	13.2 (±0.8)
	1965-2095	60.7 (±3.5)	21.1 (±1.2)

hPa was, on average, somewhat larger than that observed.

The multi-model mean ozone-induced erythemal radiation shows an increase over all regions, maximising in around 2000 in Antarctica, and followed by a reduction through the 21ˢᵗ century. In the NH extra-tropics, erythemal radiation recovers to 1960 levels by 2020–2040, while in the Antarctic it does not recover to these levels until the end of the century, and in the tropics, erythemal radiation begins to increase again in the latter part of the century.

The CCMVal-2 REF-B2 simulations show a fairly large spread in stratospheric ozone flux into the troposphere. The observations do little to constrain the range, and it is difficult to discern which models are better.

Below are model-by-model results that emphasize mainly the instances in which each model is significantly different from the multi-model mean.

AMTRAC3 performs better than average in the SH and worse than average in the NH based on the *u, v, T* metrics. It exhibits anomalously strong cooling of the Antarctic vortex in spring compared to observations.

CAM3.5 performs worse than average in the NH and about average in the SH based on the *u, v, T* metrics.

CCSRNIES performs worse than average in the stratosphere and troposphere of both hemispheres based on the *u, v, T* metrics. Its simulated decrease in Antarctic ozone is smaller than observations, and hence its simulated increase in SH erythemal radiation is smaller than in other models. Global stratosphere-troposphere ozone fluxes are overestimated in this model.

CMAM performs better than average in the NH and about average in the SH based on the *u, v, T* metrics. CMAM was

the only model coupled to an ocean model, but this did not have a noticeable effect on the diagnostics examined here. All the models reproduce tropospheric anomalies following the stratospheric events, but in the NH, CMAM (along with some other models) showed noticeably longer persistence of the anomalies compared with the observations. Its SAM index is too persistent compared to observations in both the troposphere and the stratosphere. It exhibits anomalously strong cooling of the Antarctic vortex in spring compared to observations.

E39CA performs worse than average in the stratosphere and about average in the troposphere, based on the *u, v, T* metrics.

CNRM-ACM performs very poorly in the stratosphere, and about average in the troposphere, based on the *u, v, T* metrics. Its stratospheric jets are displaced too far equatorward. CNRM-ACRM has larger than average tropical ozone losses (Section 9.3.4), and hence a larger increase in tropical UV. It is also the model with the largest negative radiative forcing due to ozone changes.

EMAC performs about average overall based on the *u, v, T* metrics. EMAC simulates too weak a stratospheric cooling in the Antarctic vortex in spring and also simulates an Antarctic total ozone trend that is too weak. It exhibits positive tropopause radiative forcing in ~2000 associated with stratospheric ozone changes.

GEOSCCM performs very well in the stratosphere based on the *u, v, T* metrics. Tropospheric skill was generally close to average, except that NH tropospheric variability was simulated somewhat poorly. This model exhibits realistic SAM time scales in the troposphere and the strato-

sphere, but its NAM time scales are somewhat too long. Moreover, in both hemispheres lower stratospheric annular mode anomalies exhibit too much persistence in their coupling with annular mode anomalies at 10 hPa. Stratosphere-troposphere ozone fluxes in this model exhibit particularly good agreement with observations.

LMDZrepro performs poorly in its simulation of synoptic variability in both hemispheres, it is about average in its simulation of other aspects of NH climate and below average in its simulation of other aspects of SH climate, based on u, v, T metrics. In both hemispheres, lower stratospheric annular mode anomalies exhibit too much persistence in their coupling with annular mode anomalies at 10 hPa in this model, and its annular mode indices are themselves too persistent in both hemispheres, in both the troposphere and stratosphere.

MRI exhibits about average performance based on the u, v, T metrics. MRI simulates larger than average increases in erythemal radiative associated with ozone depletion, and it also simulates a larger than average negative radiative forcing. It exhibits anomalously large stratosphere-troposphere ozone fluxes, particularly in the NH.

NiwaSOCOL simulates mean climate in the NH better than average, and realistic synoptic variability in the troposphere, but poor synoptic variability in the stratosphere, based on the u, v, T metrics. It exhibits a relatively large negative radiative forcing due to ozone.

SOCOL simulates NH stratosphere mean conditions well, and in other aspects is about average, based on the u, v, T metrics. It exhibits anomalously weak Antarctic ozone depletion, and hence weaker than average ozone-induced increases in SH erythemal radiation. It exhibits positive tropopause radiative forcing in ~2000 associated with stratospheric ozone changes. It exhibits anomalously high stratosphere-troposphere ozone fluxes.

ULAQ underperforms in all categories of climate: in the stratosphere and troposphere, over both hemispheres, and in mean climate as well as in interannual variability based on the u, v, T metrics. ULAQ simulates much lower stratosphere-troposphere ozone fluxes than observed, and has the largest bias in ozone fluxes compared to the observations.

UMSLIMCAT exhibits about average performance in its simulation of mean tropospheric climate, and tropospheric and stratospheric variability, but below average performance in its simulation of stratospheric variability, based on the u, v, T metrics.

UMUKCA-METO is one of the best models at simulating means and variability in the troposphere, and performs better than average in the stratosphere, based on the u, v, T metrics. This model simulates too weak a stratospheric cooling in the Antarctic stratosphere in spring.

UMUKCA-UCAM exhibits among the best simulation of tropospheric mean climate and variability, and is about average in its simulation of stratospheric mean climate and variability, based on the u, v, T metrics. It simulates too weak a stratospheric cooling in the Antarctic stratosphere in spring.

WACCM performs poorly in the u, v, T metrics for the SH, but about average in the NH. Its tropospheric synoptic variability is particularly realistic in both hemispheres. WACCM has among the most realistic (shortest) SAM time scales, but among the least realistic (longest) NAM time scales.

10.5.2 Overall Summary

This chapter has examined the dynamical, radiative and chemical effects of the stratosphere on the troposphere in the CCMVal-2 models. Stratospheric ozone changes will not greatly alter the global-mean surface warming. However, Antarctic climate as well as the global distribution of surface UV radiation are expected to be affected significantly.

An examination of the mean climate and variability in the CCMVal-2 models showed that they exhibit a much more realistic stratospheric climate than the CMIP3 climate models, and more realistic interannual variability in the troposphere. CCMVal-2 models exhibit a slight but non-significant reduction in biases compared to the earlier generation CCMVal-1 models. CCMVal-2 models simulate a downward propagation of annular mode anomalies in both hemispheres similar to that observed, with realistic ensemble-mean annular mode variances through the troposphere and stratosphere. However, the peak in variability associated with the break-down of the vortex consistently occurs too late in the year in both hemispheres in the CCMVal-2 models, and the simulated SAM tends to be too persistent through the troposphere and stratosphere in summer.

Over the period 1960-2000 the CCMVal-2 models simulate a spring cooling of the Antarctic polar vortex, and a decrease in Antarctic geopotential height which descends to the troposphere in December-February, and is associated with an intensification and southward shift of the mid-latitude jet. The amount of Antarctic ozone depletion in each model is closely correlated with its poleward shift in midlatitude jet location, amount of broadening of

the Hadley Cell, and its increase in SH tropopause height. The models indicate that in the 21ˢᵗ century, the effects of ozone recovery and GHG increases largely cancel leading to little change in jet location, tropopause height, or Hadley Cell width in the SH in summer. The effect of stratospheric ozone changes on the NAM in the CCMVal-2 models appears to be weak but significant.

Stratospheric ozone changes in the CCMVal-2 models lead to an increase in SW forcing and a decrease in LW forcing at the tropopause. However, while the ensemble mean net forcing change due to ozone changes between 1960-2000 is negative, consistent with that reported by IPCC (2007), some models show a positive net tropopause radiative forcing due to stratospheric ozone changes over this period. Erythemal ultraviolet irradiance, calculated based on CCMVal-2 ozone changes, exhibits an increase throughout the globe in the last decades of the 20ᵗʰ century. In the 21ˢᵗ century, decreasing chemical depletion is likely to contribute to a decrease in erythemal irradiance globally, while changes in the Brewer-Dobson circulation will tend to enhance the decrease in the Arctic and slow or reverse the decrease in the tropics and Antarctic. Changes in cloudiness and tropospheric ozone and aerosols are uncertain and may also be important drivers of regional surface UV change.

In the CCMVal-2 simulations ozone depletion causes a small global decrease in the stratosphere-troposphere ozone flux in the 20ᵗʰ century, and its recovery contributes to the 21ˢᵗ century increase. However, a strengthening of the Brewer-Dobson circulation is projected to be the dominant driver of an increase in stratosphere-to-troposphere ozone fluxes in the 21ˢᵗ century.

References

Arblaster, J. M., and G. A. Meehl, 2006. Contributions of external forcings to Southern Annular Mode trends, *J. Climate*, **19**, 2896–2905.

Appenzeller, C., J. Holton, and K. Rosenlof, Seasonal variation of mass transport across the tropopause, 1996. *J. Geophys. Res.* **101**, 15,071–15,078.

Baldwin, M. P., and T. J. Dunkerton, 1999. Downward propagation of the Arctic Oscillation from the stratosphere to the troposphere, *J. Geophys. Res.*, **104**, 30,937–30,946.

Baldwin, M. P. and T. J. Dunkerton, 2001. Stratospheric harbingers of anomalous weather regimes, *Science*, **244**, 581–584.

Baldwin, M. P., D. B. Stephenson, D. W. J. Thompson, T. J. Dunkerton, A. J. Charlton, and A. O'Neill, 2003. Stratospheric memory and extended-range weather forecasts, *Science*, **301**, 636–640.

Baldwin, M. P., and D. W. J. Thompson, 2009. A critical comparison of stratosphere-troposphere coupling indices, *Quart. J. Royal. Meteorol. Soc.*, **135**, 1661-1672.

Butchart, N., A. A. Scaife, M. Bourqui, J. de Grandpre, S. H. E. Hare, J. Kettleborough, U. Langematz, E. Manzini, F. Sassi, K. Shibata, D. Shindell, and M. Sigmond, 2006: Simulations of antropogenic change in the strength of the Brewer-Dobson circulation, *Clim. Dyn.*, **27**, doi: 10.1007/s00382-006-0162-4.

Coughlin, K., and K.-K. Tung, 2001. QBO Signal found at the extratropical surface through Northern Annular Modes. *Geophys. Res. Lett.*, **28**, 4563–4566.

Crook, J. A., N. P. Gillett, S. P. E. Keeley, 2008. Sensitivity of Southern Hemisphere climate to zonal asymmetry in ozone, *Geophys. Res. Lett.*, **35**, doi:10.1029/2007GL032698.

Denman, K. L., G. Brasseur, A. Chidthaisong, P. Ciais, P. M. Cox, R. E. Dickinson, D. Hauglustaine, C. Heinze, E. Holland, D. Jacob, U. Lohmann, S. Ramachandran, P. L. da Silva Dias, S. C. Wofsy and X. Zhang, 2007. Couplings Between Changes in the Climate System and Biogeochemistry. In: *Climate Change 2007: The Physical Science Basis. Contribution of Working Group I to the Fourth Assessment Report of the Intergovernmental Panel on Climate Change,* Cambridge University Press, Cambridge, United Kingdom and New York, NY, USA.

Edwards, J. M. and A. Slingo, 1996. Studies with a flexible new radiation code. I: Choosing a configuration for a large-scale model, *Quart. J. Royal. Meteorol. Soc.*, **122**, 689-719.

Eyring, V., D. W. Waugh, G. E. Bodeker, E. Cordero, H. Akiyoshi, J. Austin, S. R. Beagley, B. A. Boville, P. Braesicke, C. Brühl, N. Butchart, M. P. Chipper_eld, M. Dameris, R. Deckert, M. Deushi, S. M. Frith, R. R. Garcia, A. Gettelman, M. A. Giorgetta, D. E. Kinnison, E. Mancini, E. Manzini, D. R. Marsh, S. Matthes, T. Nagashima, P. A. Newman, J. E. Nielsen, S. Pawson, G. Pitari, D. A. Plummer, E. Rozanov, M. Schraner, J. F. Scinocca, K. Semeniuk, T. G. Shepherd, K. Shibata, B. Steil, R. S. Stolarski, W. Tian, and M. Yoshiki, 2007. Multi-model projections of ozone recovery in the 21ˢᵗ century, *J. Geophys. Res.*, **112**, doi:10.1029/2006JD008332.

Fioletov, V. E., and T. G. Shepherd, 2003. Seasonal persistence of midlatitude total ozone anomalies, *Geophys. Res. Lett.*, **30**, doi:10.1029/2002GL016739.

Forster, P., V. Ramaswamy, P. Artaxo, T. Berntsen, R. Betts, D. W. Fahey, J. Haywood, J. Lean, D. C. Lowe, G. Myhre, J. Nganga, R. Prinn, G. Raga, M. Schulz and R. Van Dorland, 2007. Changes in Atmospheric Constituents and in Radiative Forcing. In: *Climate Change 2007: The Physical Science Basis. Contribution of Working Group I to the Fourth Assessment Report of the Intergovernmental Panel on Climate Change*. Cambridge University Press, Cambridge, United Kingdom and New York, NY, USA.

Forster, P. M. F., R. S. Freckleton and K. P. Shine, 1997. On aspects of the concept of radiative forcing, *Clim. Dyn.*, **13**, 547-560.

Forster, P. and K. Shine, 1997. Radiative forcing and temperature trends from stratospheric ozone changes. *J. Geophys. Res.* **102**, 1084.

Gerber, E. P., M. P. Baldwin, H. Akiyoshi, J. Austin, S. Bekki, P. Braesicke, N. Butchart, M. Chipperfield, M. Dameris, S. Dhomse,. S. M. Frith, R. R. Garcia, H. Garny, A. Gettelman, S. C. Hardiman, M. Marchand, O. Morgenstern, J. E. Nielsen, S. Pawson, T. Peter, D. A. Plummer, J. A. Pyle, E. Rozanov, J. F. Scinocca, T. G. Shepherd, and D. Smale, 2010. Stratosphere-Troposphere Coupling and Annular Mode Variability in Chemistry-Climate Models, *J. Geophys. Res.*, doi:10.1029/2009JD013770, in press.

Gerber, E. P., L. M. Polvani, and D. Ancukiewicz, 2008. Annular mode time scales in the Integovernmental Panel on Climate Change Fourth Assessment Report models. *Geophys. Res. Lett.*, **35**, doi:10.1029/2008GL035712.

Gillett, N., and D. W. J. Thompson, 2003. Simulation of recent southern hemisphere climate change. *Science*, **302**, 273–275.

Graf, H.-F., J. Perlwitz and I. Kirchner, 1994. Northern Hemisphere tropospheric mid-latitude circulation after violent volcanic eruptions, *Contr. Atm. Phys.*, **67**, 3–13.

Grise, K. M., D. W. J. Thompson and P. M. Forster, 2009. On the role of radiative processes in stratosphere-troposphere coupling, *J. Clim.*, **22**, 4154-4161.

Hamilton, K. P., 2007. Analyses of IPCC Climate Model Data at IPRC, *IPRC Climate Newsletter*, **7**.

Hegglin, M. I., and T. G. Shepherd, 2009. Large climate-induced changes in ultraviolet index and stratosphere-to-troposphere ozone flux, *Nature Geosci.*, **2**, 687–691.

Herman, J. R., and E. A. Celarier, 1997. Earth surface reflectivity climatology at 340 nm to 380 nm from TOMS data, *J. Geophys. Res.*, **102**, 28,003-28,011.

Holton, J., P. Haynes, M. McIntyre, A. Douglass, R. Rood, and L. Pfister, 1995. Stratosphere-Troposphere Exchange, *Rev. Geophys.*, **33**, 403-439.

IPCC, 2007: Climate Change 2007: The Physical Science Basis. Contribution of Working Group I to the Fourth Assessment Report of the Intergovernmental Panel on Climate Change [Solomon, S., D. Qin, M. Manning, Z. Chen, M. Marquis, K.B. Averyt, M.Tignor and H.L. Miller (eds.)]. Cambridge University Press, Cambridge, United Kingdom and New York, NY, USA.

Ineson, S., and A. A. Scaife, 2009. The role of the stratosphere in the European climate response to El Niño, *Nature Geosci.*, **2**, 32-36.

Keeley, S. P. E., N. P. Gillett, D. W. J. Thompson, S. Solomon, P. M. de F. Forster, 2007. Is Antarctic climate most sensitive to ozone depletion in the mid or lower stratosphere? *Geophys. Res. Lett.*, **34**, doi:10.1029/2007GL031238.

Karpechko, A. Yu., N. P. Gillett, G. J. Marshall, and A. A. Scaife, 2008. Stratospheric influence on circulation changes in the southern hemisphere troposphere in coupled climate models, *Geophys. Res. Lett.*, **35**, doi:10.1029/2008GL035354.

Kinne, S., M. Schulz, C. Textor, S. Guibert, Y. Balkanski, S. E. Bauer, T. Berntsen, T. F. Berglen, O. Boucher, M. Chin, W. Collins, F. Dentener, T. Diehl, R. Easter, J. Feichter, D. Fillmore, S. Ghan, P. Ginoux, S. Gong, A. Grini, J. Hendricks, M. Herzog, L. Horowitz, I. Isaksen, T. Iversen, A. Kirkevåg, S. Kloster, D. Koch, J. E. Kristjansson, M. Krol, A. Lauer, J. F. Lamarque, G. Lesins, X. Liu, U. Lohmann, V. Montanaro, G. Myhre, J. Penner, G. Pitari, S. Reddy, O. Seland, P. Stier, T. Takemura, and X. Tie, 2006. An AeroCom initial assessment - optical properties in aerosol component modules of global models, *Atmos. Chem. Phys.*, **6**, 1815-1834.

Kodera, K., K. Yamazaki, M. Chiba and K. Shibata, 1990. Downward propagation of upper stratospheric mean

zonal wind perturbation to the troposphere, *J. Meteor. Soc. Japan,* **9**, 1263–1266.

Kodera, K., and K. Yamazaki, 1994. A possible influence of recent polar stratospheric coolings on the troposphere in the northern hemisphere winter, *Geophys. Res. Lett.*, **21**, 809–812.

Lu, J., G. A. Vecchi, and T. E. Reichler, 2007. Expansion of the Hadley cell under global warming. *Geophys. Res. Lett.*, **34**, doi:10.1029/2006GL028443.

Lal, M., A. K. Jain, and M. C. Sinha, 1987. Possible climatic implications of depletion of Antarctic ozone, *Tellus*, **39B**, 326-328.

Li, F., Stolarski, R. S., and Newman, P. A., 2009. Stratospheric ozone in the post-CFC era. *Atmos. Chem. Phys.*, **9**, 2207-2213.

Manzini, E., B. Steil, C. Brühl, M. A. Giorgetta, and K. Krüger, 2003. A new interactive chemistry-climate model: 2. Sensitivity of the middle atmosphere to ozone depletion and increase in greenhouse gases and implications for recent stratospheric cooling, *J. Geophys. Res.*, **108**, doi:10.1029/2002JD002977.

Marshall, G. J., P. A. Stott, J. Turner, W. M. Connolley, J. C. King, and T. A. Lachlan-Cope, 2004. Causes of exceptional atmospheric circulation changes in the Southern Hemisphere, *Geophys. Res. Lett.*, **31**, doi:10.1029/2004GL019952.

Mayer, B., and A. Kylling, 2005. Technical note: The libRadtran software package for radiative transfer calculations - description and examples of use, *Atmos. Chem. Phys.*, **5**, 1855-1877.

McLandress, C., and T. G. Shepherd, 2009. Simulated anthropogenic changes in the Brewer-Dobson circulation, including its extension to high latitudes, *J. Clim.*, **22**, 1516-1540.

McPeters, R. D., G. J. Labow, and J. A. Logan, 2007. Ozone climatological profiles for satellite retrieval algorithms, *J. Geophys. Res.*, **112**, doi:10.1029/2005JD006823.

Meehl, G. A., C. Covey, T. Delworth, M. Latif, B. McAvaney, J. F. B. Mitchell, R. J. Stouffer, and K. E. Taylor, 2007a. The WCRP CMIP3 multimodel dataset: A new era in climate change research. *Bull. Amer. Meteor. Soc.*, **88**, 1383-1394.

Meehl, G. A., T. F. Stocker, W. D. Collins, P. Friedlingstein, A. T. Gaye, J. M. Gregory, A. Kitoh, R. Knutti, J. M. Murphy, A. Noda, S. C. B. Raper, I. G. Wat-

terson, A. J. Weaver and Z.-C. Zhao, 2007b. Global Climate Projections. In: *Climate Change 2007: The Physical Science Basis. Contribution of Working Group I to the Fourth Assessment Report of the Intergovernmental Panel on Climate Change*. Cambridge University Press, Cambridge, United Kingdom and New York, NY, USA.

Morgenstern, O., H. Akiyoshi, S. Bekki , P. Braesicke , N. Butchart, M. Chipperfield , A. Gettelman, D. Cugnet, M. Deushi, S. S. Dhomse, R. R. Garcia, N. P. Gillett, S. C. Hardiman , J. Jumelet, D. E. Kinnison, J.-F. Lamarque , F. Lott, M. Marchand, M. Michou, T. Nakamura, D. Olivié, S. Pawson, T. Peter, D. Plummer, J. A. Pyle, E. Rozanov , D. Saint-Martin, J. F. Scinocca, K. Shibata, M. Sigmond, D. Smale, H. Teyssèdre, W. Tian, A. Voldoire, and Y. Yamashita, 2010. Anthropogenic forcing of the Northern Annular Mode in CCMVal-2 models, *J. Geophys. Res.*, doi:10.1029/2009JD013347, in press.

Olsen, M. A., M. R. Schoeberl, and A. R. Douglass, 2004. Stratosphere-troposphere exchange of mass and ozone. *J. Geophys. Res.*, **109**, doi:10.1029/2004JD005186.

Polvani L. M., and D. W. Waugh, 2004. Upward wave activity flux as precursor to extreme stratospheric events and subsequent anomalous surface weather regimes , *J. Climate*, **17**, 3548–3554.

Ramanathan, V., 1977. Troposphere-stratosphere feedback mechanism: Stratospheric warming and its effect on the polar energy budget and the tropospheric circulation. *J. Atmos. Sci.*, **34**, 439–447.

Randel, W. J., and F. Wu, 1999. Cooling of the Arctic and Antarctic polar stratosphere due to ozone depletion. *J. Climate,* **12**, 1467-1479.

Reichler, T. and J. Kim, 2008. How well do coupled models simulate today's climate? *Bull. Amer. Meteor. Soc.*, **89**, 303-311.

Rind, D., J. Lean, J. Lerner, P. Lonergan, and A. Leboissitier, 2008. Exploring the stratospheric/tropospheric response to solar forcing, *J. Geophys. Res.*, **113**, doi:10.1029/2008JD010114.

Robock, A., and J. Mao, 1992. Winter warming from large volcanic eruptions, *Geophys. Res. Lett.*, **12**, 2405–2408.

Santer, B. D., T. M. L. Wigley, J. S. Boyle, D. J. Gaffen, J. J. Hnilo, D. Nychka, D. E. Parker, and K. E. Taylor,

2000. Statistical significance of trends and trend differences in layer-average atmospheric temperature time series, *J. Geophys. Res.*, **105**, 7337–7356.

Santer, B. D., M. F. Wehner, T. M. L. Wigley, R. Sausen, G. A. Meehl, K. E. Taylor, C. Ammann, J. Arblaster, W. M. Washington, J. S. Boyle, and W. Bruggemann, 2003. Contribution of anthropogenic and natural forcing to recent tropopause height changes, *Science*, **301**, 479483.

Seidel, D. J., Q. Fu, W. J. Randel, and T. J. Reichler, 2008. Widening of the tropical belt in a changing climate, *Nature Geoscience*, **1**, 21-24.

Shepherd, T. G., 2008. Dynamics, stratospheric ozone, and climate change. *Atmos.-Ocean,* **46**, 117-138.

Shindell, D. T., and G. A. Schmidt, 2004. Southern Hemisphere climate response to ozone changes and greenhouse gas increases, *Geophys. Res. Lett.*, **31**, doi:10.1029/2004GL020724.

Son, S.-W., L. M. Polvani, D. W. Waugh, H. Akiyoshi, R. Garcia, D. Kinnison, S. Pawson, E. Rozanov, T. G. Shepherd, and K. Shibata, 2008. The impact of stratospheric ozone recovery on the Southern Hemisphere westerly jet, *Science*, **320**, 1486-1489.

Son, S.-W., L. M. Polvani, D. W. Waugh, T. Birner, H. Akiyoshi, R. R. Garcia, A. Gettelman, D. A. Plummer, and E. Rozanov, 2009a. The impact of stratospheric ozone recovery on tropopause height trends , *J. Clim.*, **22**, 429-445.

Son S.-W., N. F. Tandon, L. M. Polvani, and D. W. Waugh, 2009b. The ozone hole and southern hemisphere climate change, *Geophys. Res. Lett.*, **36**, doi:10.1029/2009GL038671.

Stenchikov, G. L., I. Kirchner, A. Robock, H.-F. Graf, J. C. Artuna, R. G. Grainger, A. Lambert, and L. Thomason, 1998. Radiative forcing from the 1991 Mount Pinatubo volcanic eruption, *J. Geophys. Res.*, **103**, 13,837–13,857.

Stenchikov, G., K. Hamilton, A. Robock, and V. Ramaswamy, and M.D. Schwarzkopf, 2004. Arctic oscillation response to the 1991 Pinatubo eruption in the SKYHI general circulation model with a realistic quasi-biennial oscillation. *J. Geophys. Res.*, **109**, doi: 10.1029/2003JD003699.

Stevenson, D. S., R. M. Doherty, M. G. Sanderson, W. J. Collins, C. E. Johnson, and R. G. Derwent, 2004. Radiative forcing from aircraft NOx emissions: Mecha-

nisms and seasonal dependence, *J. Geophys. Res.*, **109**, doi:10.1029/2004JD004759.

Stevenson, D. S., F. J. Dentener, M. G. Schultz, K. Ellingsen, T. P. C. van Noije, O. Wild, G. Zeng, M. Amann, C. S. Atherton, N. Bell, D. J. Bergmann, I. Bey, T. Butler, J. Cofala, W. J. Collins, R. G. Derwent, R. M. Doherty, J. Drevet, H. J. Eskes, A. M. Fiore, M. Gauss, D. A. Hauglustaine, L. W. Horowitz, I. S. A. Isaksen, M. C. Krol, J.-F. Lamarque, M. G. Lawrence, V. Montanaro, J.-F. Müller, G. Pitari, M. J. Prather, J. A. Pyle, S. Rast, J. M. Rodriguez, M. G. Sanderson, N. H. Savage, D. T. Shindell, S. E. Strahan, K. Sudo, S. Szopa, 2006. Multi-model ensemble of present-day and near-future tropospheric ozone. *J. Geophys. Res.*, **111**, doi:10.1029/2005JD006338.

Thompson, D. W. J, and J. M. Wallace, 1998. The Arctic Oscillation signature in the wintertime geopotential height and temperature fields, *Geophys. Res. Lett.*, **25**, 1297–1300.

Thompson, D. W. J., and J. M. Wallace, 2000. Annular modes in the extratropical circulation. Part I: Month-to-month variability, *J. Clim.*, **13**, 1000–1016.

Thompson, D. W. J., M. P. Baldwin, and J. M. Wallace, 2002. Stratospheric connection to northern hemisphere wintertime weather: Implications for prediction, *J. Climate*, **15**, 1421–1428.

Thompson, D. W. J., and S. Solomon, 2002. Interpretation of recent southern hemisphere climate change. *Science*, **296**, 895–899.

Thompson, D. W. J., M. P. Baldwin, and S. Solomon, 2005. Stratosphere-troposphere coupling in the southern hemisphere. *J. Atmos. Sci.*, **62**, 708–715.

Tourpali, K., A. F. Bais, A. Kazantzidis, C. S. Zerefos, H. Akiyoshi, J. Austin, C. Brühl, N. Butchart, M. P. Chipperfield, M. Dameris, M. Deushi, V. Eyring, M. A. Giorgetta, D. E. Kinnison, E. Mancini, D. R. Marsh, T. Nagashima, G. Pitari, D. A. Plummer, E. Rozanov, K. Shibata, and W. Tian, 2009. Clear sky UV simulations in the 21st century based on ozone and temperature projections from Chemistry-Climate Models, *Atmos. Chem. Phys.*, **9**, 1165-1172**.**

Uppala, S.M., P.W. Kållberg, A.J. Simmons, U. Andrae, V. Da Costa Bechtold, M. Fiorino, J.K. Gibson, J. Haseler, A. Hernandez, G.A. Kelly, X. Li, K. Onogi, S. Saarinen, N. Sokka, R.P. Allan, E. Andersson, K. Arpe, M.A. Balmaseda, A.C.M. Beljaars, L. Van De

Berg, J. Bidlot, N. Bormann, S. Caires, F. Cheval-
lier, A. Dethof, M. Dragosavac, M. Fisher, M. Fuen-
tes, S. Hagemann, E. Hólm, B.J. Hoskins, L. Isak-
sen, P.A.E.M. Janssen, R. Jenne, A.P. Mcnally, J.-F.
Mahfouf, J.-J. Morcrette, N.A. Rayner, R. W. Saun-
ders, P. Simon, A. Sterl, K.E. Trenberth, A. Untch,
D. Vasiljevic, P. Viterbo, and J. Woollen, 2005. The
ERA-40 reanalysis, *Quart. J. Royal. Meteorol. Soc.*,
131, 2961–3012.

Waugh, D. W., L. Oman, P. A. Newman, R. S. Stolarski, S.
Pawson, J. E. Nielsen, and J. Perlwitz, 2009. Effect
of zonal asymmetries in stratospheric ozone on simu-
lated Southern Hemisphere climate trends , *Geophys.
Res. Lett.*, **36**, L18701, doi:10.1029/2009GL040419.

World Meteorological Organisation Scientific assessment
of ozone depletion, Global Ozone Res. Monit. Rep.
16, Geneva, 1992.

World Meteorological Organization (WMO)/United Na-
tions Environment Programme (UNEP), 2007. *Sci-
entific Assessment of Ozone Depletion: 2006*, World
Meteorological Organization, Global Ozone Re-
search and Monitoring Project, Report No. 50, Ge-
neva, Switzerland.